EUMETSAT Contract Report

EUMETSAT EUM/CO/22/4600002673/SDM

Contract Report to EUMETSAT

Evaluation of the EPS-Sterna 325 GHz channels in the Ensemble of Data Assimilations

Report for EUMETSAT contract no. EUM/CO/22/4600002673/SDM

Katie Lean and Niels Bormann
April 2024

Contents

Abstract

The proposed EPS-Sterna constellation of small satellites will carry a microwave (MW) sounding instrument comprising frequencies around 50-60 GHz and 183 GHz with a long heritage of use in Numerical Weather Prediction (NWP) but will also include a novel set of four humidity-sounding channels at 325 GHz. These higher, sub-millimetre MW frequencies have not been flown before on a space-borne platform. To allow evaluation of their additional benefit for NWP, a strategy is developed here to simulate and assimilate the 325 GHz channels in an all-sky framework.

A key aspect of this strategy is that observation error modelling has been adapted for the new 325 GHz channels. The model follows the usual all-sky observation error model of assigning larger errors in cloudy regions, but uses a new cloud indicator which exploits the cloud signal extracted from the lowest peaking 325 GHz channel. Compared to using the scattering index employed for the 183 GHz humidity-sounding channels, the model with the new cloud indicator leads to a more Gaussian distribution when considering background departures normalised by the assigned observation error.

EDA experiments show that the 325 GHz channels produce a similar positive impact as the 183 GHz channels when each channel set is added separately to the temperature sounding channels at 50 GHz. When added on top of the 50 GHz and 183 GHz sounding channels, the impact of the 325 GHz channels is mostly neutral, with some benefits for relative humidity in the mid-troposphere. Some inflation of the observation errors assigned to the 325 GHz channels is found necessary to achieve this impact. It is hypothesised that this is due to the presence of neglected observation error correlations, and better handling of these may be required to realise more benefit from the combined channel set in the future.

1 Introduction

Current microwave (MW) sounders and imagers provide a vital contribution to forecast accuracy (Bormann et al., 2019) but do not yet exploit the sub-millimetre spectral range (equivalent to frequencies above 300 GHz but below infrared). At these higher frequencies, the greater sensitivity to ice hydrometeors enables improved characterisation of ice clouds. Future missions are planned to include these frequencies such as the Ice Cloud Imager (ICI, to be launched on Metop-Second Generation) which has primary objectives to validate ice cloud models and improve the parametrisation of ice clouds (Bell et al., 2017). The MW sounding instrument proposed for the small satellite platforms that form the future EPS-Sterna constellation will also exploit four novel channels at 325 GHz in addition to a set of well-established frequencies around 50-60 GHz and 183 GHz. Motivation for including a set of four channels around 325 GHz on EPS-Sterna platforms arose primarily from a study by Eriksson et al. (2020) which demonstrated potential benefit e.g. for cloud characterisation. However, there has so far been little quantitative evaluation of the expected impact on Numerical Weather Prediction (NWP).

In earlier work, the Ensemble of Data Assimilations (EDA) method was used to evaluate the expected future impact of the EPS-Sterna constellation, excluding the 325 GHz channels (Lean et al., 2023). The assessment suggested significant positive impact from the EPS-Sterna constellation using only the 50 and 183 GHz bands relative to both the impact of existing MW and an entire multi-sensor Metop platform. Here, we focus on the additional benefit from the suite of 325 GHz channels. As these are new frequencies for a space-borne platform, a strategy for simulating and assimilating the new frequencies must first be developed. The EDA technique can then be employed to investigate the relative impacts of separately assimilating the two humidity bands (183 GHz or 325 GHz) and the more complex case of combining all three frequency bands at 50, 183 and 325 GHz.

The 325 GHz channels exploit a water vapour absorption band while the higher frequency brings more sensitivity to ice hydrometeors than currently used humidity sounding channels at 183 GHz (e.g., Evans

and Stephens, 1995; Eriksson et al., 2017). Channels around 325 GHz have not been flown before on a space-borne platform and their assimilation hence needs to be developed to predict their future impact. The future ICI instrument will cover frequencies from 183 GHz up to 664 GHz, including three channels around 325 GHz. In part motivated by this upcoming launch, preparations have been underway to effectively use these submillimetre frequencies such as emissivity modelling (e.g., Wang et al., 2017; Dinnat et al., 2023) and radiative transfer calculations (e.g., Eriksson et al., 2017; Geer et al., 2021; Turner et al., 2022). Here, we can take advantage of these recent developments to use in the evaluation of EPS-Sterna. In addition to ICI, experience with real data from the 325 GHz channels should be possible in the near future from the Arctic Weather Satellite (AWS) due to be launched in 2024 (a single small satellite pathfinder platform carrying the same instrument as proposed for the EPS-Sterna constellation).

In developing a strategy to effectively use 325 GHz there are several considerations including ensuring the accuracy of surface emissivity estimates and quality control choices, for instance, for using the data over difficult snow/sea-ice surfaces. The 325 GHz channels will also be used within the all-sky framework which means that the corresponding configuration for generating observation errors must be defined. In the all-sky observation error model, the assigned error is increased in the presence of cloudy signals in either the observations or model to account for different representativeness of clouds (Geer et al., 2010, 2017). For real MW data, an appropriate cloud indicator is chosen for each assimilated instrument channel to estimate the strength of the cloudy signals in both observations and model. The cloud indicator chosen for the 325 GHz channels will need to take into account the additional sensitivity to ice scattering for these channels.

Our assimilation strategy for the 325 GHz channels is tested here within the EDA framework. We will first investigate the addition of the 325 GHz channels instead of the 183 GHz channels available on EPS-Sterna. The aim is to demonstrate a beneficial use of these channels and to intercompare the relative benefits of these two channel sets when they are combined with temperature channels around the 50-60 GHz band. This is a useful first step to establish confidence in the simulation and assimilation choices and that there is potential for positive impact with the 325 GHz channels. Subsequently, EDA experiments combine all three channel sets to assess the benefit of using the whole instrument on each platform. A novel aspect of this is that it significantly increases the number of MW humidify-sounding channels assimilated from a single sensor with a total of nine channels, compared to the current use of three channels from the Microwave Humidity Sounder (MHS) instrument and five channels from the MicroWave Humidity Sounder – 2 (MWHS-2) instrument. This increase in the number of humidity channels may bring new challenges, for instance in terms of handling representation error which tends to be dominant for these channels and may be correlated between different channels. The benefit of the 325 GHz channels in addition to the 183 GHz channels is expected to primarily come from a better characterisation of ice clouds, an aspect that will be a new test for all-sky assimilation.

The structure of the report is as follows: Section 2 investigates the suitability of the surface emissivity model at higher frequencies while section 3 considers screening choices, drawing from the experience with the existing configuration for the 183 GHz channels. In section 4, we will develop the observation error model for the 325 GHz channels, based on the use of a new cloud indicator adapted to these channels. EDA experiments which compare the benefit of the 325 GHz and 183 GHz respectively when added to the temperature sounding channels are presented in section 5 while the results from combining all the frequency bands are shown in section 6. Lastly, a summary and future work are discussed in section 7.

2 Surface emissivity for 325 GHz

Where MW sounding channels have a sensitivity to the surface, accurate estimates of surface emissivity are required to successfully assimilate the observations (e.g., English, 1999; Dinnat et al., 2023). As part of the fast radiative transfer model employed at ECMWF for assimilating MW radiances, RTTOV-SCATT[1] (version 13.0), a FAST microwave Emissivity Model, FASTEM (version 6), is applied over oceans (English and Hewison, 1998; Kazumori and English, 2015). FASTEM was not optimised for frequencies above 200 GHz and an improved model, SURFace Fast Emissivity Model for Ocean (SURFEM-

---

[1]RTTOV = Radiative Transfer for TOVS, TOVS = TIROS Operational Vertical Sounder, TIROS = Television Infrared Observation Satellite
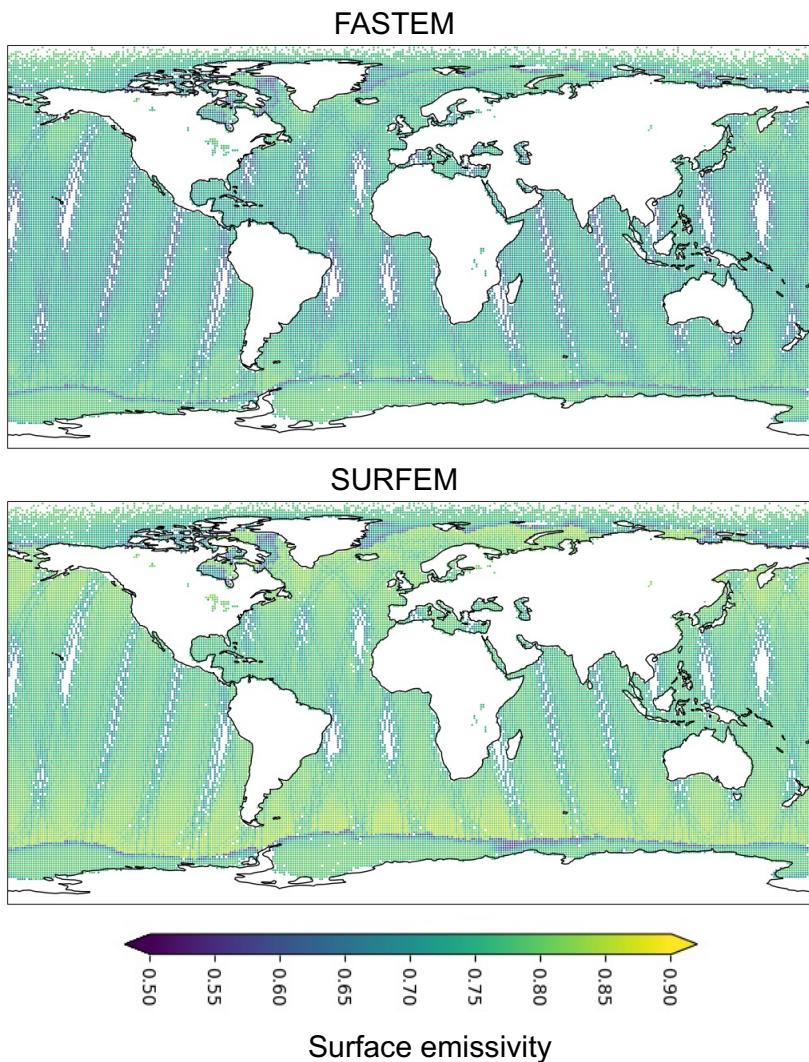

Figure 1: Map showing ocean surface emissivity for the 325±6.6 GHz channel (lowest peaking 325 GHz) channel using the FASTEM-6 model (top panel) and SURFEM-Ocean (bottom panel). Data are for a representative 12-hour window from one EPS-Sterna satellite and have not been subject to any quality control.

Ocean), available in the latest RTTOV release (version 13.2), now incorporates a larger frequency range, up to 700 GHz, amongst other improvements (Kilic et al., 2023). SURFEM-Ocean will be used operationally at ECMWF from cycle 49R1 onwards (Geer et al., 2024), but the system used in EDA experiments to evaluate the EPS-Sterna scenarios does not support the use of SURFEM-Ocean yet. However, for the purposes of understanding any potential limitations of applying FASTEM to the 325 GHz channels in future simulation and EDA experiments, testing is conducted here using a newer cycle of the Integrated Forecast System (IFS). Characteristics of simulated brightness temperatures (BTs) and surface emissivity values are compared when generated using either the FASTEM or SURFEM-Ocean models while keeping all other settings the same.

Figure 1 demonstrates a clear offset in the emissivity values for the lowest peaking 325±6.6 GHz channel when using the different emissivity models, which is similarly observed in the high peaking 325 GHz
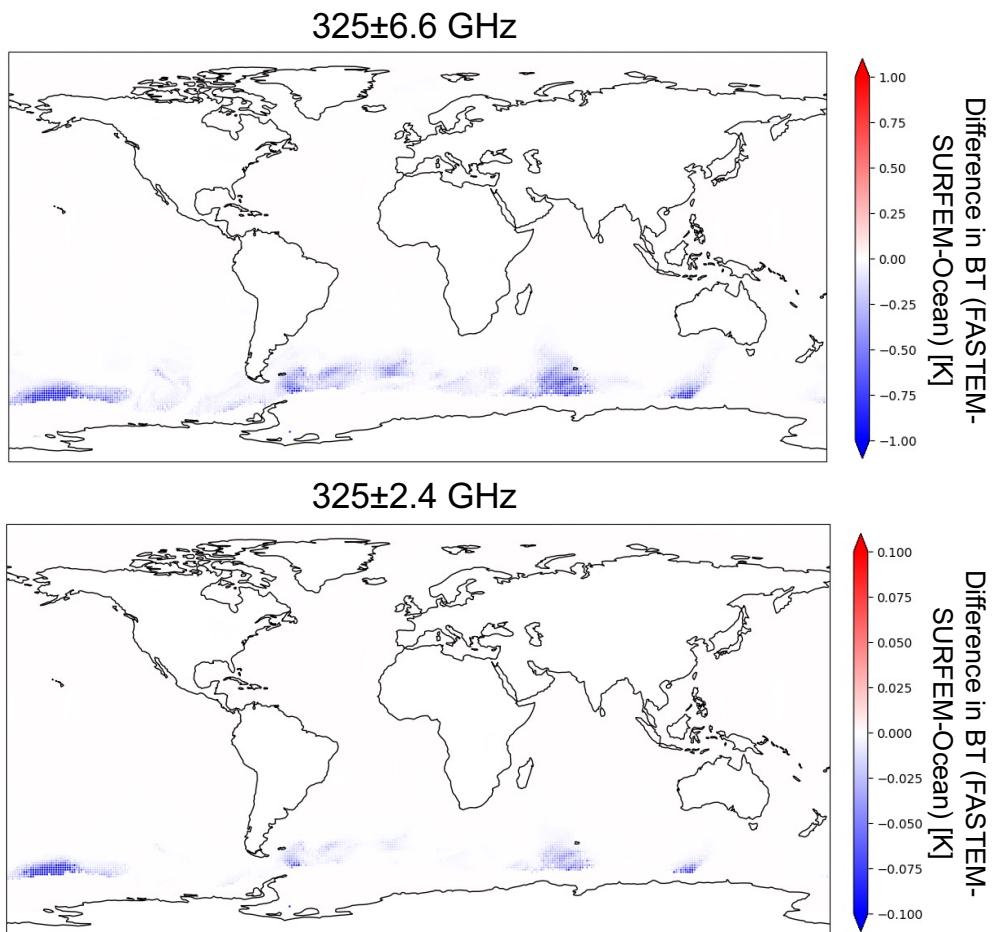
Figure 2: Map showing the difference in simulated BTs over ocean as a result of using the FASTEM-6 or SURFEM-Ocean emissivity model for the 325±6.6 channel (lowest peaking) (top panel) and 325±2.4 channel (second highest peaking) (bottom panel). Blue colours indicate larger BTs values are simulated when using SURFEM-Ocean – note that different colour scale limits are employed in the two maps. Data are for a representative 12-hour window from one EPS-Sterna satellite and have not been subject to any quality control.

channels. The SURFEM-Ocean model on average produces values around 0.05 higher than FASTEM. However, when considering the simulated BTs generated with these respective emissivity inputs, Fig. 2 reveals that these relatively large changes in emissivity in the lowest peaking channel translate to little difference overall in BT. Larger differences in BT are localised to the Southern Ocean where dry atmospheric conditions lead to higher surface-sensitivity for this channel. The changes are likely related to improvements in SURFEM-Ocean that better account for higher wind speeds (Kilic et al., 2023). For the higher peaking 325 GHz channels (e.g. Fig. 2, lower panel) differences in BT are very small (generally <0.05 K). The relatively small change in the simulated BTs suggests that any impacts on the EPS-Sterna evaluation using the EDA technique would have little sensitivity to the emissivity model for the 325 GHz frequencies. Note that, as expected, differences for lower frequency channels on the EPS-Sterna instrument also showed little difference in either emissivity or BT simulation.

Over land, the surface emissivity is taken from an atlas, Tool to Estimate Land Surface Emissivity from Microwave to Submillimetre Waves (TELSEM^2), to simulate the observation. TELSEM^2 comprises a climatology of monthly emissivity estimates that have been recently extended up to frequencies of 700 GHz in preparation for the upcoming ICI mission (Wang et al., 2017). In practice, this results in the same emissivity values being used for both 183 and 325 GHz channels. However, emissivity varies relatively little at these higher microwave frequencies (e.g., Weng, 2011) allowing the application of retrievals from the available window channels to the higher frequencies. Over the more difficult snow/sea-ice surfaces, we apply the same crude estimate of the emissivity during the simulation step as for lower frequencies (following details summarised in Lean et al., 2022a). In this instance, for mixed scenes, the surface emissivity is calculated as a weighted mean of the emissivities of the contributing surfaces, using the model surface fractions to determine the weights. During the later assimilation of the 325 GHz channels over land/snow/sea-ice, a dynamic emissivity retrieval is performed following the same strategy as 183 GHz, again exploiting the low variation of emissivity in the higher MW frequencies. Over snow-free land, 89 GHz is used for the retrieval while 165.5 GHz is used over snow/sea-ice. A comparison of the dynamically retrieved emissivity for 183 and 325 GHz confirmed that sensible values were used for 325 GHz (not shown). Improved treatment of the difficult snow/sea-ice surfaces is an active area of research and will allow improved use of surface sensitivity MW observations in the future. Note that screening choices (discussed in the next section) currently restrict the use of channels with high surface sensitivity in these difficult regions.

3   Quality control choices for 325 GHz

It is possible to draw parallels between each 325 GHz channel and an equivalent 183 GHz channel. Using the weighting functions described in Eriksson et al. (2020) (their Fig. 8), which indicate the vertical profiles of sensitivity to each layer of the atmosphere, a 325 GHz channel can be paired with a 183 GHz channel that has the closest weighting function match. This results in pairings of channels as described in Table 1. Figure 3 illustrates the good agreement in features seen for similar peaking weighting functions for the lowest peaking 325 GHz (325±6.6 GHz) and 2nd lowest peaking 183 GHz (178.811 GHz) channels. In clear-sky conditions, BTs are very close between the two channels while in cloudier regions, larger depressions in BT are present at 325±6.6 GHz. In quality control procedures employed for 183 GHz, lower peaking channels have more restrictions, to avoid larger surface-emissivity errors over difficult surfaces. For future assimilation, screening choices developed for 183 GHz will be applied to the correspondingly matched channels from the 325 GHz channels. Table 2 details key screening choices for the 325 GHz and 183 GHz channels.
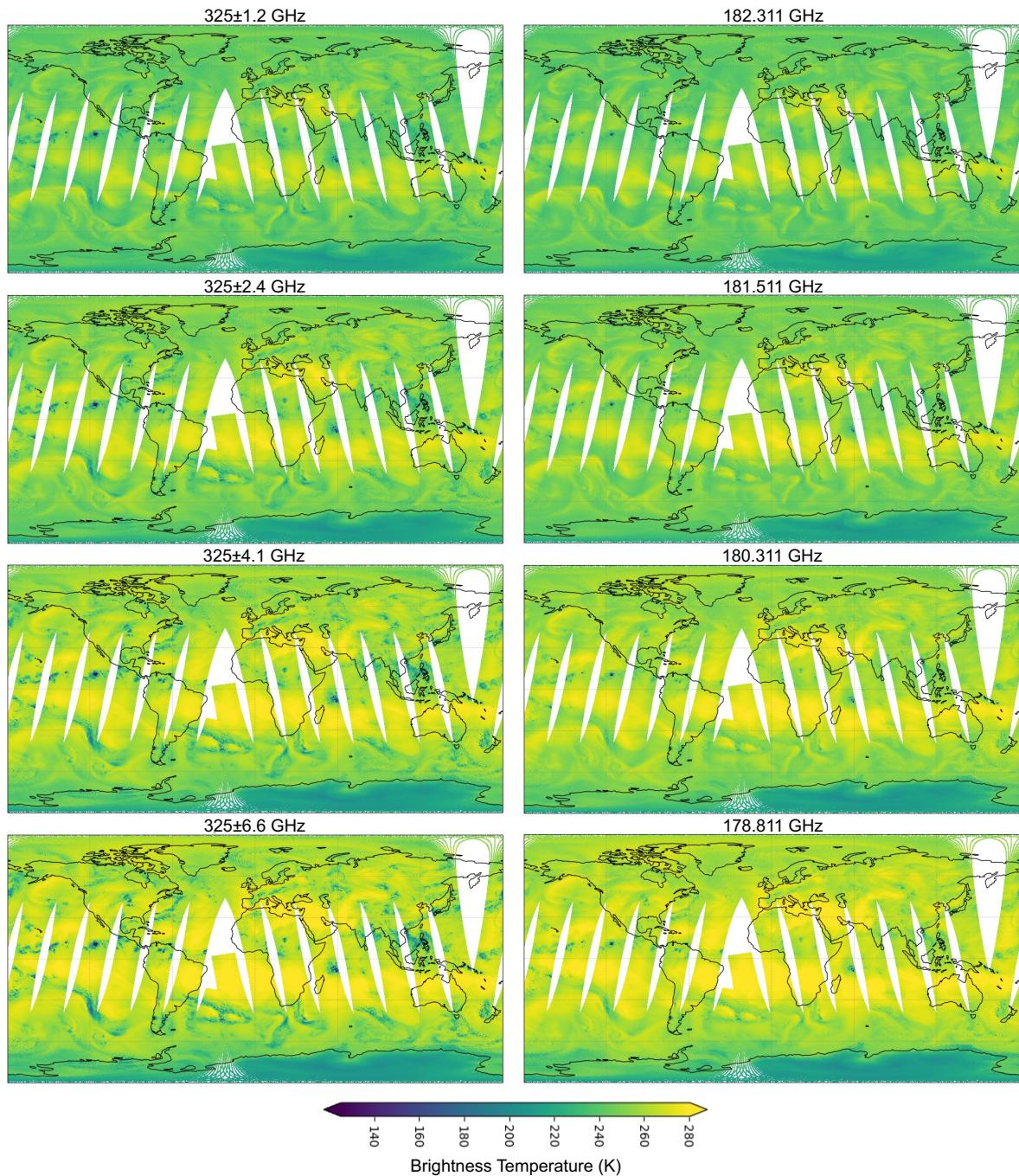
Figure 3: Maps showing simulated BTs for the 325 GHz channels (left column) and corresponding 183 GHz channels (right column). Each row shows channel pairs with similar vertical sensitivity as outlined in Table 1 with the height of the peak in weighting function decreasing from top to bottom row. Data are from one EPS-Sterna satellite for 09-21Z 1 July 2019

Table 1: Frequency and corresponding channel number on the EPS-Sterna instrument for 183 and 325 GHz channel pairs that have been matched by the best agreement in weighting function.

Pair number	183 GHz		325 GHz	
	Channel number	Frequency (GHz)	Channel number	Frequency (GHz)
1	12	178.811	19	325±6.6
2	13	180.311	18	325±4.1
3	14	181.511	17	325±2.4
4	15	182.311	16	325±1.2

Table 2: Summary of key quality control choices made in the assimilation of the 183 and 325 GHz channels. A check-mark indicates which regions are rejected for the given channels.

Screening	Frequency (GHz)			
	178.811, 325±6.6	180.311, 325±4.1	181.511, 325±2.4	182.311, 325±1.2
Orography>1000m	✓	✓		
Orography>1500m			✓	✓
Polar regions (>60°N/S)	✓			
Coast	✓			
Snow/sea-ice/sea surface < 274K	✓			

4   Adaptation of the all-sky observation error model

We will now adapt the all-sky observation error model for the new 325 GHz channels. This all-sky observation error model reflects that representation errors are larger in the presence of clouds (Geer et al., 2010, 2017), and this is modelled as a function of a cloud indicator indicating the presence of cloudy signals from either the observations or the background. Assigned values increase from a minimum clear-sky value to a maximum cloudy value. The model reflects that the standard deviation of observation – background BT (O-B, where the background is a short-range forecast, after bias correction) increase with increasing presence of clouds. For the EPS-Sterna 183 GHz channels, the cloud indicator is constructed by a scattering index formed by the difference in BT at 89 and 165.5 GHz (following the strategy for the Microwave Humidity Sounder (MHS) where equivalent frequencies, 89 and 157 GHz, are used). This exploits a difference in the scattering from precipitation-sized ice particles (Geer et al., 2014). Equation 1 and 2 provide the formulation of the scatter index over the land and ocean respectively:

$$C_{land}^{89-165.5} = BT_{89} - BT_{165.5} \tag{1}$$

$$C_{ocean}^{89-165.5} = (BT_{89} - BT_{165.5}) - (BT_{89}^{clr} - BT_{165.5}^{clr}) \tag{2}$$

where BT_{89} and $BT_{165.5}$ are the BTs at 89 and 165.5 GHz respectively while BT_{89}^{clr} and $BT_{165.5}^{clr}$ are the corresponding BTs at the same frequencies calculated for clear-sky conditions. To generate estimates

for the clear-sky scenario at the same location, the model equivalent BT is calculated using the clear-sky version of the radiative transfer model. Over ocean, it is necessary to remove the clear-sky component due to the water vapour absorption also causing large BT differences which mask signals from cloud. Over each surface, the scatter index is calculated using observed BTs, $C_{obs}^{89-165.5}$, and model background BT equivalents $C_{bkgrd}^{89-165.5}$. The average of these is taken to form the symmetric cloud indicator, $C_{sym}^{89-165.5}$:

$$C_{sym}^{89-165.5} = (C_{obs}^{89-165.5} + C_{bkgrd}^{89-165.5})/2 \tag{3}$$

The minimum clear-sky error and maximum cloudy error are determined empirically for real MW data. For 183 GHz channels on the EPS-Sterna instrument, formulae derived from existing MW data are applied that link the Noise Equivalent Delta Temperature (NEDT) for each channel to the respective minimum clear-sky value (further details in Lean et al., 2022b, reproduced for convenience in appendix A). Due to similar instrument characteristics, the same maximum values from the real MW data, using MHS as a basis, were retained for the 183 GHz channels on the EPS-Sterna instrument in Lean et al. (2023).

While the scatter index formulation discussed above has been used successfully for 183 GHz, the inclusion of 325 GHz channels allows the possibility of exploiting further ice scattering information as part of the observation error model. In the following, we look at selecting a suitable cloud indicator for the 325 GHz channels and describe the strategy to define minimum and maximum error values. The potential for updating the 183 GHz error model is also discussed.

4.1   Cloud indicator for 325 GHz

The 325 GHz channels provide greater sensitivity to smaller ice particles than their 183 GHz counterparts (e.g., Eriksson et al., 2020; Kaur et al., 2021), as previously highlighted in Fig. 3. To capture this, we investigate here a cloud indicator for the 325 GHz channels that is different from the 89-165.5 GHz scatter index used for the 183 GHz channels and instead tailored to capture the cloud signals for these higher frequencies. For this indicator, we estimate the cloud signal present in the observed brightness temperatures BT_{obs} as well as the background simulations BT_{bkcld} through comparisons to clear-sky brightness temperature simulations BT_{bkclr}. The proposed new cloud indicator calculation therefore becomes:

$$C_{sym}^{325\pm6.6} = (\text{abs}(BT_{obs} - BT_{bkclr}) + \text{abs}(BT_{bkcld} - BT_{bkclr}))/2 \tag{4}$$

This uses the same structure as the cloud indicator employed for the EPS-Sterna 50 GHz temperature sounding channels (Lean et al., 2021), albeit adapted to use the lowest-peaking 325 GHz channel (325±6.6 GHz) for which the cloud signals will be largest out of the 325 GHz channels. We will contrast the characteristics of this new cloud indicator to those of the 89-165.5 GHz scatter index, in order to highlight some of the advantages. Various other cloud indicators were also investigated, such as using scatter indices between different combinations of channels or combinations of different scatter indices. However, overall, the $C_{sym}^{325\pm6.6}$ indicator is considered to work best and was hence adopted for the EDA experimentation. Further details of the investigation into other options of cloud indicators are given in appendix B.

To visualise the spatial structure of the symmetric cloud indicator, Fig. 4 illustrates the typical geographical variability using either 89-165.5 GHz (top panel) or the single channel formulation, $C_{sym}^{325\pm6.6}$ (equation 4) (lower panel). Patterns of high values (red colours) highlight similar features for both cloud

indicators, corresponding to areas of increased ice scattering. There are some differences, for example $C_{sym}^{325\pm6.6}$ suggests more presence of cloud around Indonesia. The range of cloud indicator values is also larger for $C_{sym}^{325\pm6.6}$ resulting in some localised areas of deeper red colours. Over the land there are large areas of negative values in $C_{sym}^{89-165.5}$ which are close to zero in $C_{sym}^{325\pm6.6}$, where the design ensures that values cannot be negative.
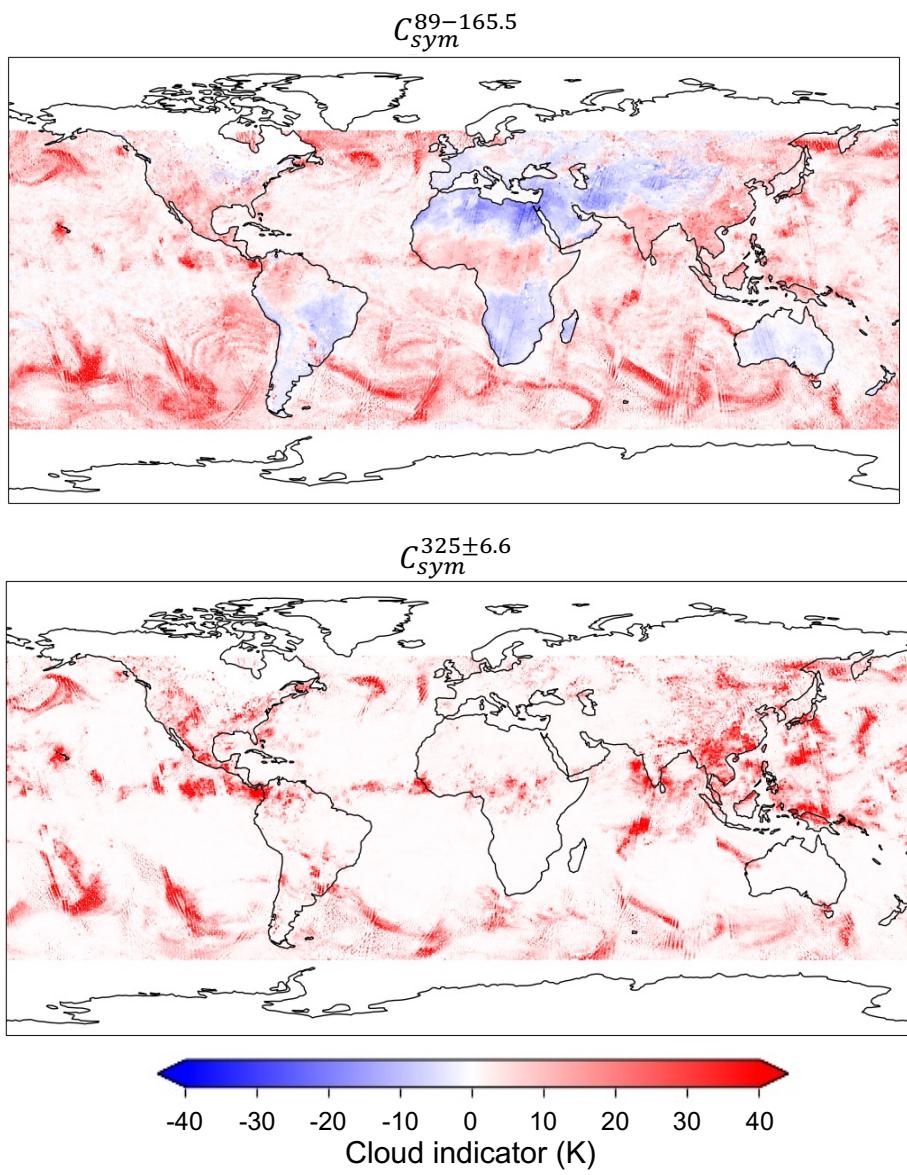
$$C_{sym}^{89-165.5}$$

$$C_{sym}^{325\pm6.6}$$

Figure 4: Map showing $C_{sym}^{89-165.5}$ (top panel) and $C_{sym}^{325\pm6.6}$ (lower panel). Redder colours indicate estimates of greater presence of cloud which would result in higher observation errors assigned to the corresponding observations. Data are for the period 17-23 July 2019 for one EPS-Sterna satellite where no screening has been applied apart from latitude limits at $\pm60°$N.

4.2 Relationship between cloud indicator and standard deviation of O-B

A successful cloud indicator in the all-sky error model should be able to identify areas with larger standard deviation of O-B associated with higher representation errors due to the presence of clouds. It also needs to indicate conditions with less cloud (i.e. low standard deviation of O-B) as more weight can be placed on the observation in the assimilation in these situations. For ease of modelling, a smooth relationship is desired between the increasing cloud signal and increasing standard deviation of O-B.

In the following, we examine the dependence of the standard deviation of O-B on the proposed cloud indicator. To do so, we use statistics taken from a 4D-Var experiment in which the simulated Sterna observations have been added, run at the same resolution as the EDA experiments presented later. Previous work found that for the 183 GHz channels, the simulated data demonstrated good agreement with real data in the characteristics of O-B and inclusion of representation errors (Lean et al., 2022b) which supports the application of a similar technique to investigate the cloud indicator suitability for the 325 GHz channels.
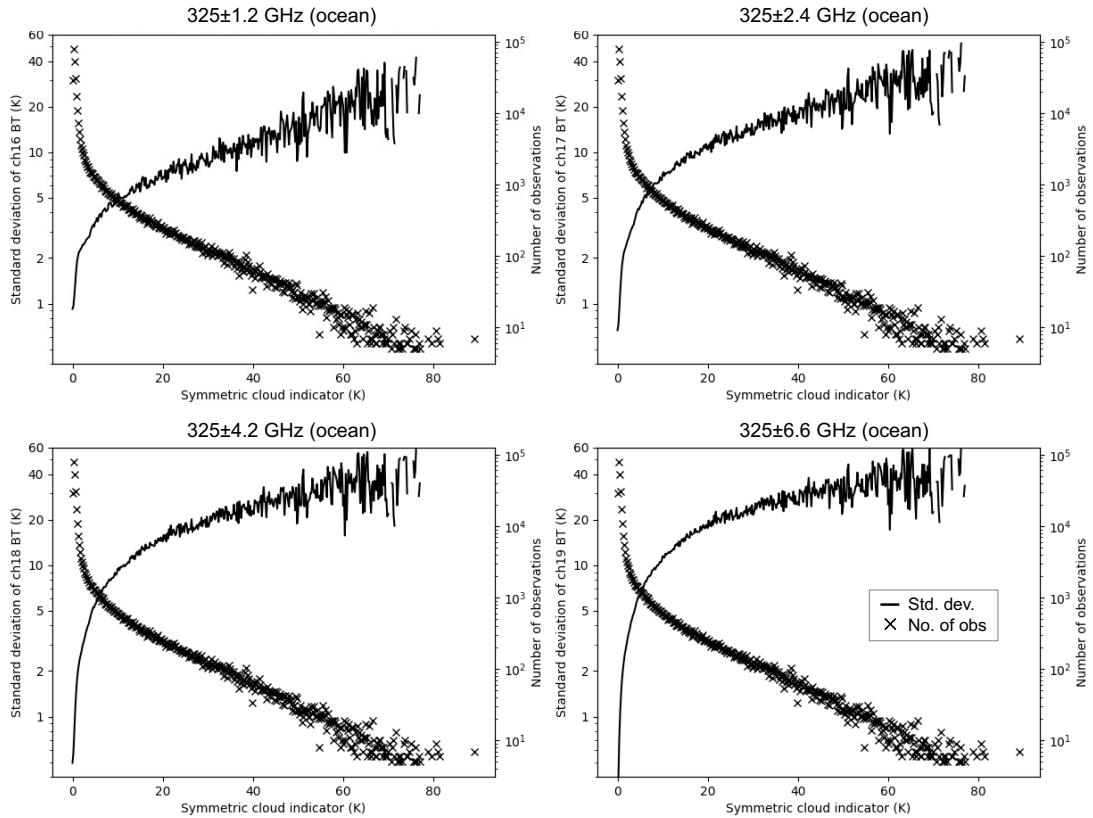

Figure 5: Standard deviation of O-B binned as a function of the cloud indicator $C_{sym}^{325\pm6.6}$. Data are for (clockwise from top left) the 325±1.2, 325±2.4 325±6.6 and 325±4.2 GHz channel, respectively. Lines show the standard deviation of O-B (left y-axis), whereas stars show the number of observations per bin (right y-axis). Data are for all observations not yet subject to quality control from an EPS-Sterna satellite for a period of seven days over ocean only, limited to ±60°N to exclude more difficult surfaces for BT simulation.
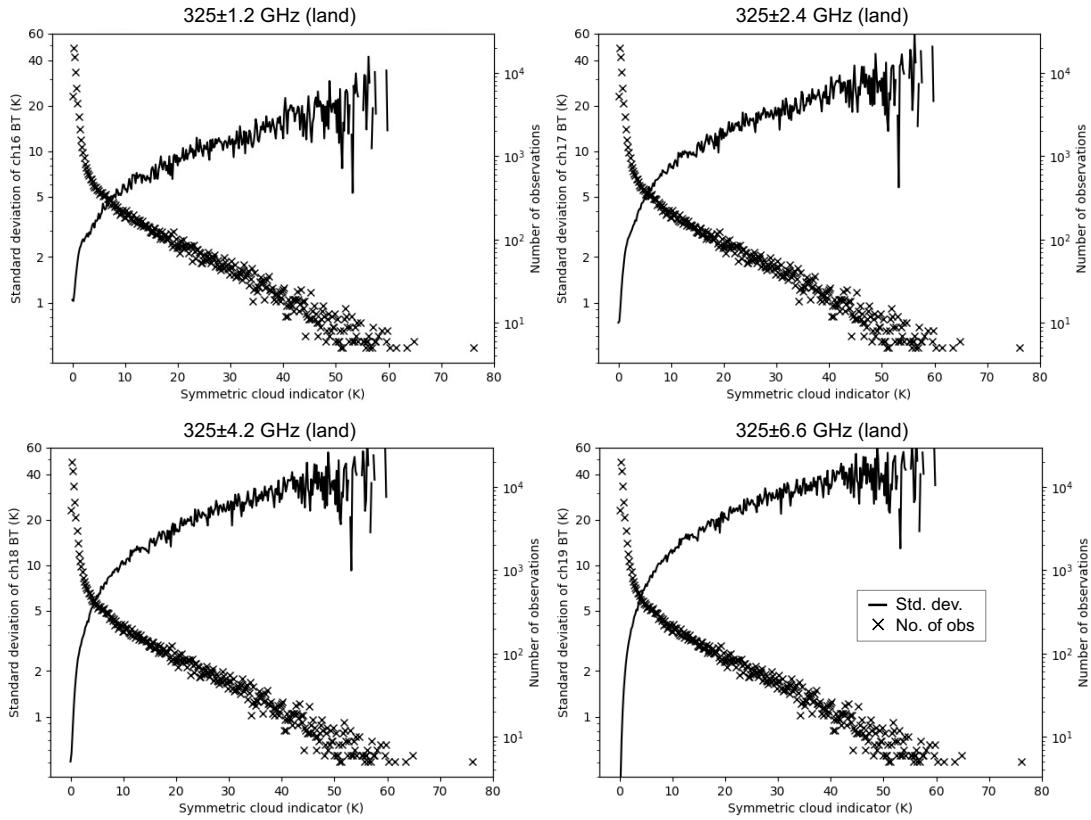
Figure 6: As for figure 5 but for land points only.

Figures 5 and 6 show the dependence of the standard deviation of O-B on $C_{sym}^{325\pm6.6}$ for the four 325 GHz channels over land and ocean, respectively. The standard deviation of (O-B) rises smoothly from a minimum value and reaches a saturation point as required. Note that for the 325±6.6 GHz channel, the design of $C_{sym}^{325\pm6.6}$ means the lowest values of $C_{sym}^{325\pm6.6}$ imply not only small cloud contributions, but also good agreement between the observations and clear-sky background equivalents, so the standard deviation of O-B tends towards zero. For the highest cloud indicator values, the standard deviation of O-B is larger for $C_{sym}^{325\pm6.6}$ than $C_{sym}^{89-165.5}$ (not shown), indicating a better ability to discriminate areas associated with such larger values.

The ability of $C_{sym}^{325\pm6.6}$ and the 89-165.5 GHz scatter index $C_{sym}^{89-165.5}$ to identify cases with larger standard deviation of O-B is further examined in Figures 7 and 8. These display the standard deviation of O-B jointly as a function of both of these cloud indicators, with the distribution of the number of cases given in Fig. 9. While the highest standard deviations of O-B for both indicators are associated with larger cloud indicator values, it is clear that the relationship between higher $C_{sym}^{325\pm6.6}$ and higher standard deviations of O-B is stronger. In contrast, there are some larger $C_{sym}^{89-165.5}$ values that are associated with relatively small standard deviations of O-B. This implies that if $C_{sym}^{89-165.5}$ was used as cloud indicator in the observation error model instead of $C_{sym}^{325\pm6.6}$ there may be data that are assigned observation errors that are too high and therefore unjustly given less weighting in the assimilation. Figures 7 and 8 also suggest that there is relatively little benefit in considering to model the standard deviation of O-B as a function of both cloud indicators, as the relationship primarily follows $C_{sym}^{325\pm6.6}$ alone. The result suggests that the sensitivities of the 89-165.5 GHz scatter index are not as well aligned with the ice scattering that
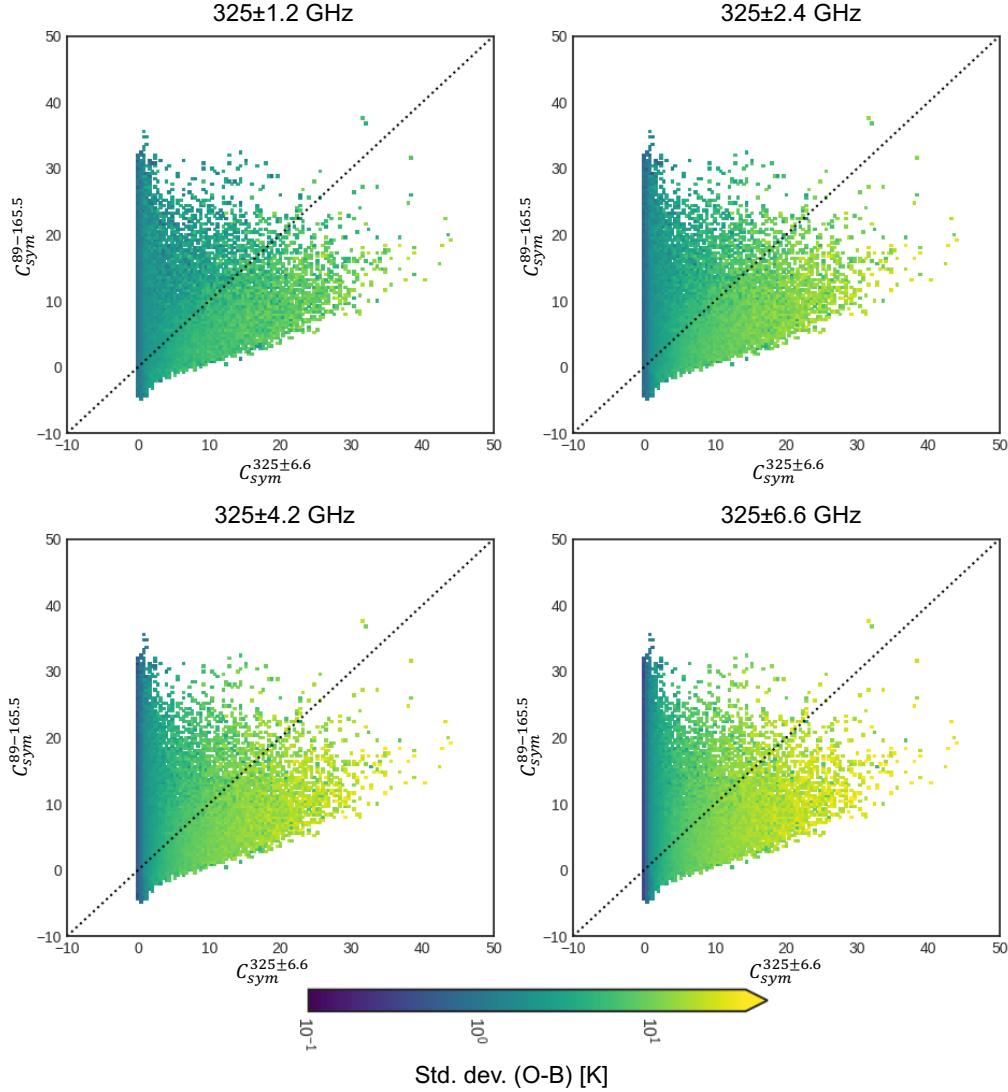
Figure 7: Standard deviation of O-B as a function of $C_{sym}^{89-165.5}$ and $C_{sym}^{325\pm6.6}$. Clockwise from top left, the data are for the 325±1.2, 325±2.4 325±6.6 and 325±4.2 GHz channel, respectively. Data are for all observations not yet subject to quality control from a single EPS-Sterna satellite for a period of seven days over ocean only limited to ±60°N.

dominates the representation errors at 325 GHz whereas using an indicator that is more tailored to these frequencies is beneficial.

Having established the usefulness of $C_{sym}^{325\pm6.6}$ for observation error modelling, we can also consider whether the observation error model for the 183 GHz channels may benefit from 325 GHz information in the cloud indicator. Figure 10 shows a representative example of the dependence of the standard deviation of O-B against $C_{sym}^{89-165.5}$ and $C_{sym}^{325\pm6.6}$. Similar to the finding for the 325 GHz channels, there is a correlation between increasing standard deviation and $C_{sym}^{89-165.5}$, but the relationship with $C_{sym}^{325\pm6.6}$ appears stronger. Again, these results suggest that some low standard deviation situations may be assigned too low weighting when using $C_{sym}^{89-165.5}$, particularly over the ocean. Redefining and tuning a
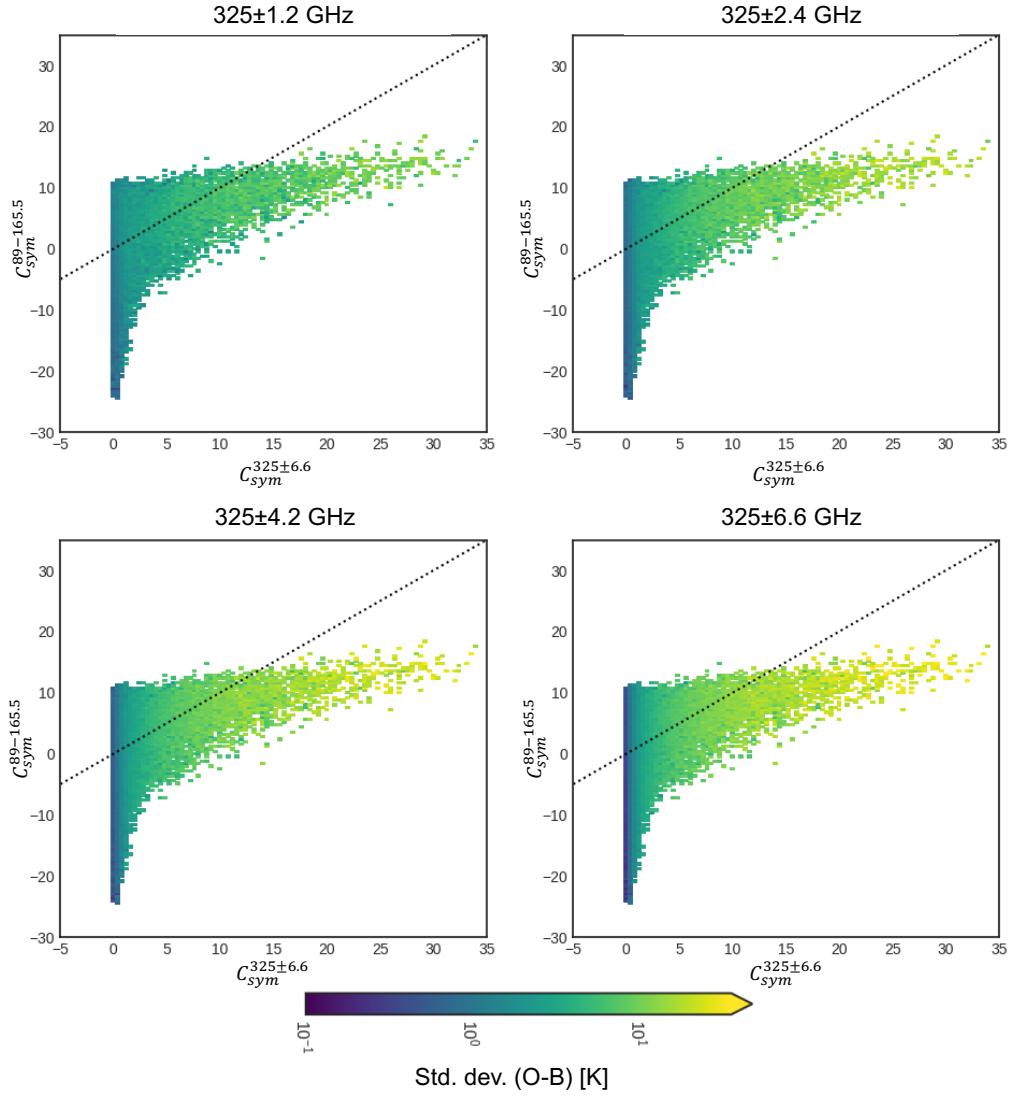
Figure 8: As for Fig. 7 but for land points only.

new error model is not a trivial task so for further experimentation in this project, we will continue to use the $C_{sym}^{89-165.5}$ indicator for the 183 GHz channels. However, there is good indication that this choice of cloud indicator may not be optimal when there is information available from 325 GHz and this could be revisited for the assimilation of real AWS/EPS-Sterna data.
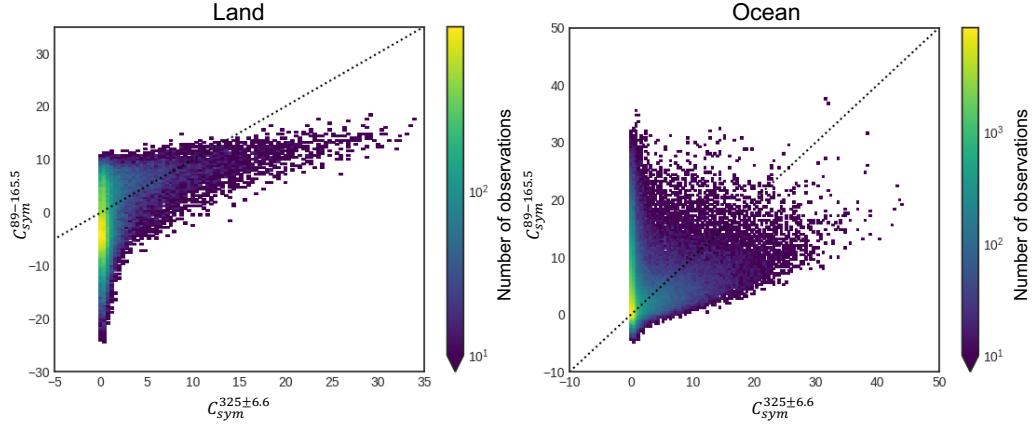
Figure 9: Number of observations as a function of $C_{sym}^{89-165.5}$ and $C_{sym}^{325\pm6.6}$, corresponding to Fig. 7 for ocean points (right panel) and Fig. 8 for land points (left panel).
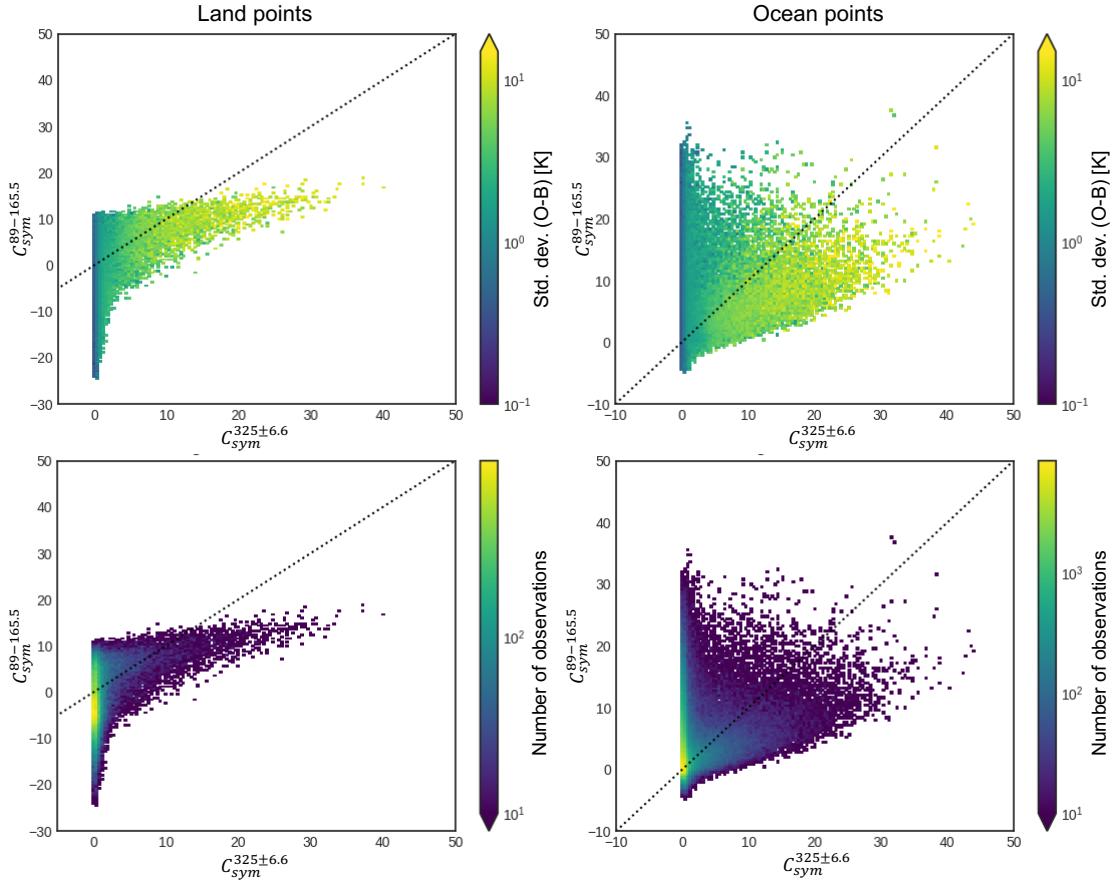
Figure 10: Distribution of standard deviation of O-B (top row) and corresponding observation density (bottom row) as a function of $C_{sym}^{89-165.5}$ and $C_{sym}^{325\pm6.6}$. Data are for the 178.811 GHz channel (second lowest peaking 183 GHz channel) over land (left column) and over ocean (right column) using all observations not yet subject to quality control from a single EPS-Sterna satellite for a period of seven days and limited to $\pm60°$N.

4.3   Setting of minimum/maximum observation errors

In the following, we will determine the minimum and maximum observation error values used in the observation error model for the 325 GHz channels, that is, the observation errors assigned in clear and cloudy regions, respectively. For channels on the EPS-Sterna instrument used in earlier EDA experiments in task 1, these values were based on those currently used for existing MW instruments. A different strategy is required for the novel 325 GHz channels, as there are no heritage observations available. Characteristics in the clear-sky situations are similar between 325 and 183 GHz channels with comparable weighting functions. Figure 11 demonstrates this similarity by comparing the relationship between the standard deviation of O-B for the lowest and highest peaking 325 GHz and their respective matched 183 GHz channels as a function of cloud indicator value. At values of C_{sym} close to zero (i.e. a clear-sky situation), the standard deviation of O-B is about the same for the matched 325 and 183 GHz channels. It hence appears justified to use the same formula and parameters derived to convert between the NEDT estimates and assumed clear-sky observation errors for the 183 GHz channels (Lean et al.,
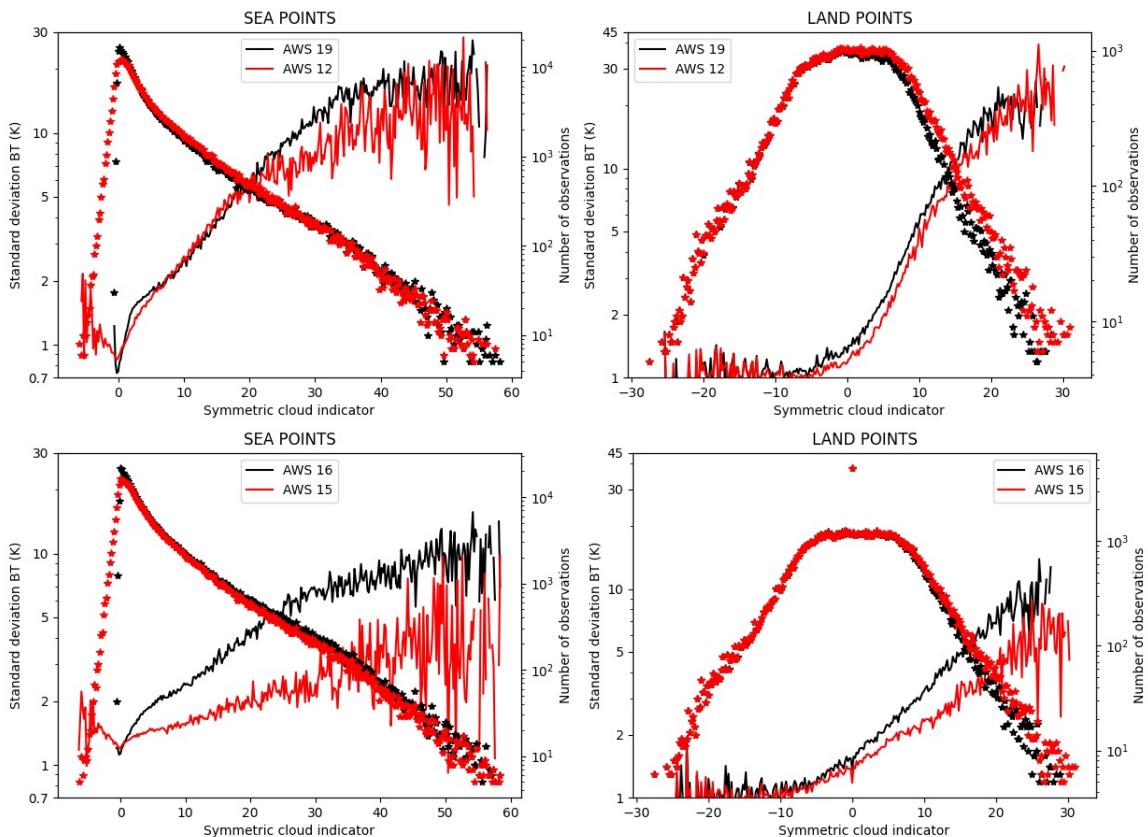

Figure 11: Standard deviation of O-B binned as a function of the cloud indicator $C_{sym}^{89-165.5}$ for selected 183 GHz (red) and 325 GHz channels (black) that peak at similar altitudes. Lines show the standard deviation of O-B (left y-axis), whereas stars show the number of observations per bin (right y-axis). The top row shows results for the lowest-peaking 178.8 GHz and 325±6.6 GHz channels, using data over sea on the left and data over land on the right (in both cases limited to ±60°N). The bottom row shows similarly results for the 182.3±1 GHz and 325±1.2 GHz channels.

Table 3: Minimum clear-sky and maximum cloudy observation errors for use in the all-sky error model using the single channel based cloud indicator for the 325 GHz channels (16-19) and equivalent values of 183 GHz channels for reference (12-15). The upper limit for the C_{sym} value (the value of the indicator that defines the saturated cloud presence) is also given. For all 183 GHz channels, the minimum value of C_{sym}, indicating clear-sky, is zero while for all 325 GHz channels the minimum is one.

Channel number	C_{sym} upper limit		Min clear error		Max cloudy error	
	Sea	Land	Sea	Land	Sea	Land
12	34	21.5	2	1.8	28	26
13	34	21.5	1.9	1.8	19.9	20
14	34	21.5	1.9	1.8	14.9	14.8
15	37	20	1.8	1.9	9.8	6.9
16	53	40	1.9	2	34.8	12.7
17	50	40	2	1.9	62.1	37.0
18	50	40	2.1	1.9	60.8	35.7
19	50	35	2.1	1.9	72	37.6

2022b). In practice, as the clear-sky error is dominated by representation error (i.e. errors arising due to differences in the humidity scales or processes represented in the model and observations), despite larger 325 GHz NEDT, clear-sky errors are only slightly larger than their 183 GHz counterparts (around 0.1 K increase to errors of around 2 K).

The maximum cloudy observation errors for the 325 GHz channels are based on those for the 183 GHz channels, scaled to account for the different cloud sensitivity. The approach has been chosen to benefit as far as possible from the empirical estimates of cloud-related representation error available from the existing 183 GHz channels. These are adopted directly from equivalent MHS channels, with extrapolation between neighbouring channels where necessary (as described in Lean et al., 2022b). Scaling of these values is introduced to account for differences in the cloud sensitivity between the two channel sets. The step is necessary as there is no prior experience with real 325 GHz data, and it aims to avoid a potential under-estimation of the cloud-related representation error for the 325 GHz channels. To calculate the scaling, the plateaus of the standard deviations of O-B for 325 GHz and matched 183 GHz channels were estimated for the EPS-Sterna data for large cloud-indicator values. The ratio of the plateaus is used as a multiplying factor for the 183 GHz maximum value to give the final value used for each 325 GHz channel. The adjustments introduced through this scaling are relatively small over land, but somewhat larger over ocean. Table 3 provides a summary of the minimum and maximum observation errors used for the 325 GHz channels, with values for the corresponding 183 GHz channels also given for reference.

4.4 Evaluation of normalised departure distributions

In the all-sky approach, the observation error model plays an important role in transforming the highly non-Gaussian distribution of the actual background departures into one that is approximately Gaussian when normalised departures are considered. Figure 12 shows that for O-B statistics that have not yet been normalised, the 325 GHz channel has stronger tails i.e. a higher number of outliers and a weaker maximum than would be expected from a Gaussian distribution. While this is also the case for the 183 GHz channels (as previously noted by Geer et al., 2014), the situation appears to be worse for the 325 GHz channels.
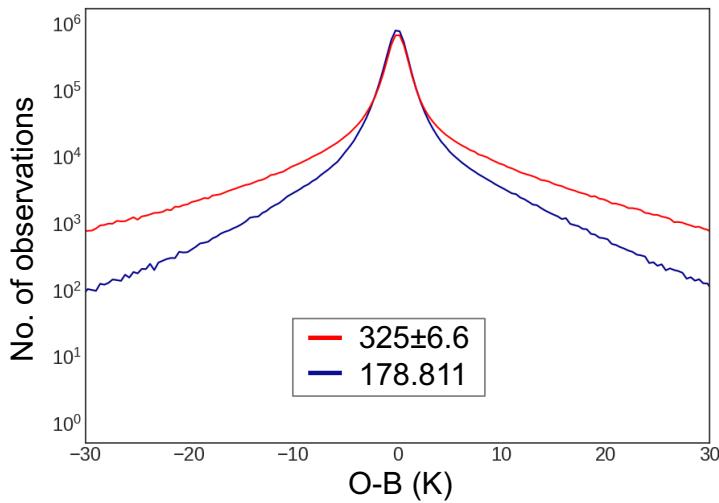
Figure 12: Probability density functions of the background departure for the lowest peaking 325±6.6 GHz and equivalent peaking 183 GHz channel (178.811 GHz). Data are for the Northern Hemisphere (lat > 20°N) for a period of 10 days 8-18 July 2019 before quality control, taken from the control member of an EDA experiment (i.e. observations are unperturbed).

As a test of the observation error model based on $C_{sym}^{325\pm6.6}$ and the parameters in Table 3, Fig. 13 examines to what extent the background departures normalised by the assigned observation error follow a Gaussian distribution. Here, representative examples are shown using the lowest and highest peaking 325 GHz channels. Dashed lines show an ideal Gaussian distribution. The good match between the red solid and dashed lines suggests that the observation error model based on $C_{sym}^{325\pm6.6}$ performs well at capturing the situation-dependence of the observation error, leading to a distribution that is very close to Gaussian. For comparison, the figure also includes results for an observation error model based on $C_{sym}^{89-165.5}$. Here, the distribution is far less Gaussian (compare solid and dashed blue lines), and the $C_{sym}^{325\pm6.6}$-based model fares much better in this respect.

5   Relative impacts of 183 and 325 GHz channels

We will now move to the evaluation of the impact of the new 325 GHz channels in the EDA. When assimilating the 325 GHz channels, there are two aspects to consider: 1) ensuring appropriate use of these new channels as alternative source of humidity-sounding information, and 2) evaluating and optimising their impact when assimilated in conjunction with other frequencies on the satellite, especially the other humidity sounding channels at 183 GHz. As there is a lot of similarity in the sensitivity of the 183 and 325 GHz channels, inter-channel error correlations are expected between equivalent channels in the two frequency bands. This aspect may bring additional challenges when the two humidity-sounding bands are used together.

As a first step, we will therefore now evaluate the use of the 325 GHz channels as the only source of humidity-sounding information, and we contrast their impact to that obtained with the more traditional 183 GHz humidity sounding channels. To do so, three EDA experiments have been run, each using the simulated six-satellite nominal EPS-Sterna constellation on top of the Baseline observing system of real observations that is described in detail in Lean et al. (2023):
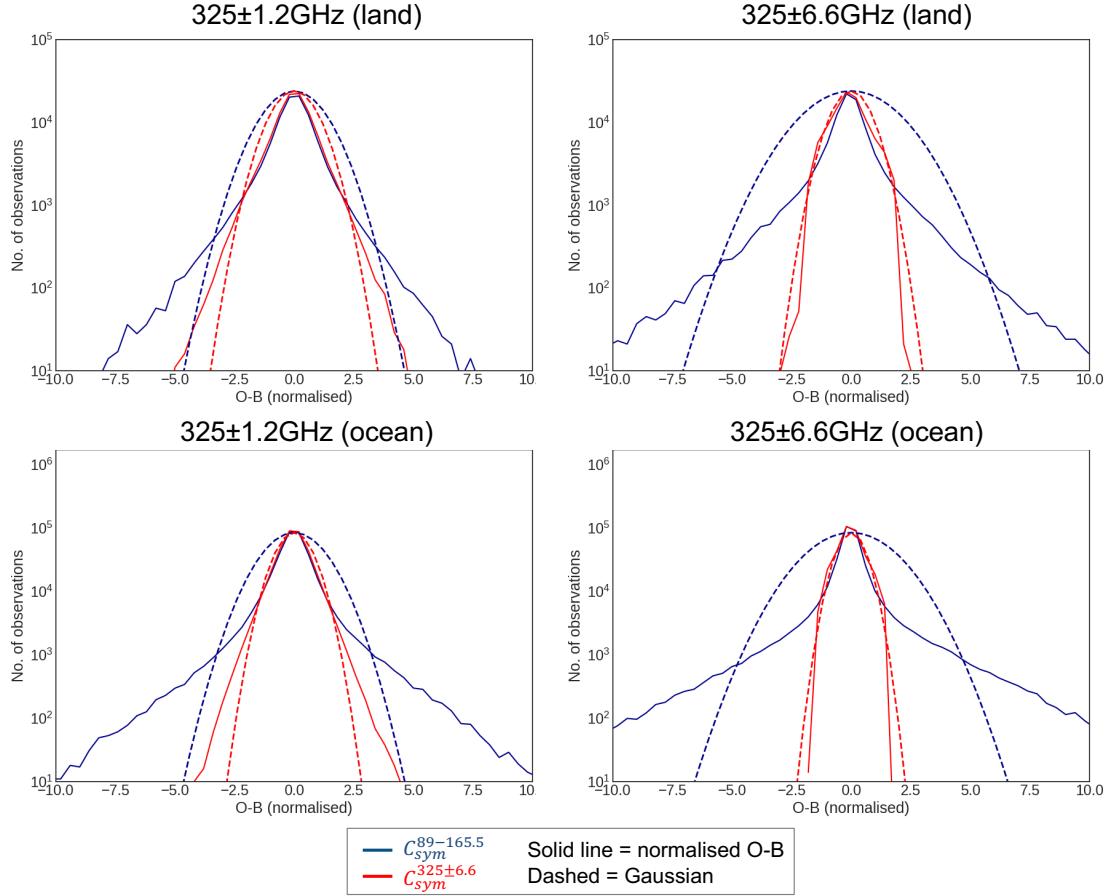
Figure 13: Probability density functions of the background departure normalised by the assigned observation error, using either $C_{sym}^{89-165.5}$ (blue) or $C_{sym}^{325\pm6.6}$ (red) as cloud indicator (solid lines). The observation error model employs the parameters derived in Table 3 for $C_{sym}^{325\pm6.6}$. The different panels show statistics for data over land (top row) and over ocean (bottom row), respectively, with the highest peaking 325±1.2 GHz in the left column and the lowest peaking 325±6.6 GHz channel in the right column. Dashed lines depict an example Gaussian curve, with the standard deviation of the underlying data for orientation. Statistics are based on a period of 7 days 17-23 July 2019 before quality control, derived from the control member of an EDA experiment (i.e. observations are unperturbed).

50only: Experiment with the Baseline real observing system plus the 50 GHz temperature-sounding channels from the 6-satellite nominal EPS-Sterna constellation.

50+325: As 50only, but with the four 325 GHz humidity-sounding channels from EPS-Sterna added.

50+4x183: As 50only, but with the highest-peaking four of the five 183 GHz channels from EPS-Sterna added. This experiment hence uses only the 183 GHz channels that have 325 GHz counterparts, to allow a better comparison to the 50+325 experiment.

All three EDA experiments use the same EDA configuration as described in Lean et al. (2023), that is, a 10-member EDA with a spatial resolution of $T_{CO}399$ ($\approx$ 25 km), run for the period 1-28 July 2019. Assimilation settings for the 50 and 183 GHz channels are also as described in Lean et al. (2023). This
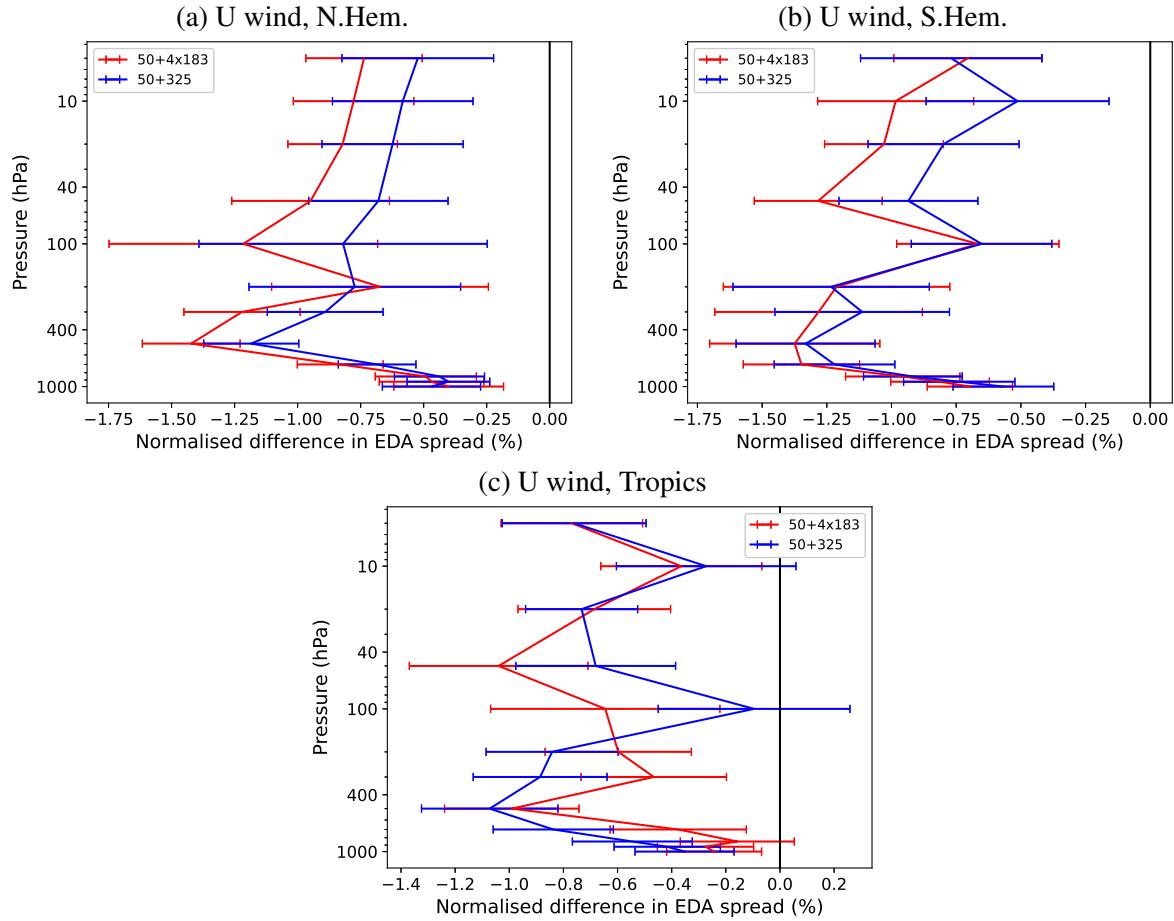
Figure 14: Vertical profiles of the EDA spread reduction for the U component of wind in the (a) Northern Hemisphere (lat > 20°N), (b) Southern Hemisphere (lat > 20°S) and (c) the Tropics (lat < ±20°N) for the 50+4x183 experiment (red) and the 50+325 experiment (blue) relative to the 50only experiment. Reductions in spread indicate benefit from the addition of the 325 GHz channels or the top-four 183 GHz channels. Data are for the period 8-28 July 2019. Horizontal bars indicate 95 % significance intervals.

includes the simulation of 3x3 averaging of 9 fields of view over 3 neighbouring scan-positions and scan-lines, prior to spatial thinning to alternating grid-points of a $T_L 255$ grid, leading to a minimum separation distance of around 111 km.

Figure 14 and 15 show representative examples of the clear significant benefit from the addition of the four 325 GHz channels to the temperature sounding channels. For wind, temperature and geopotential height, the spread reduction obtained from adding the 325 GHz channels in the 50+325 experiment is overall mostly similar to the addition of four 183 GHz to the same reference in the 50+4x183 experiment. Some subtle differences exit, such as the larger tropospheric wind impact from the 325 GHz channels in the Tropics or the weaker wind impact over the Northern Hemisphere extra-tropics (e.g., Fig. 14). Nevertheless, overall most of the impact of the 183 GHz channels is replicated by the 325 GHz channels. This is also the case for relative humidity, but the upper level humidity impact from the 325 GHz channels appears consistently a little smaller (e.g., right panel of Fig. 15). The sensitivity to ice particles at 325 GHz may impede some of the water vapour signals and therefore result in a slightly reduced impact on relative humidity when used on their own. Note that the 325 GHz channels also have slightly higher instrument noise values than the 183 GHz counterparts and this may also contribute to a lower
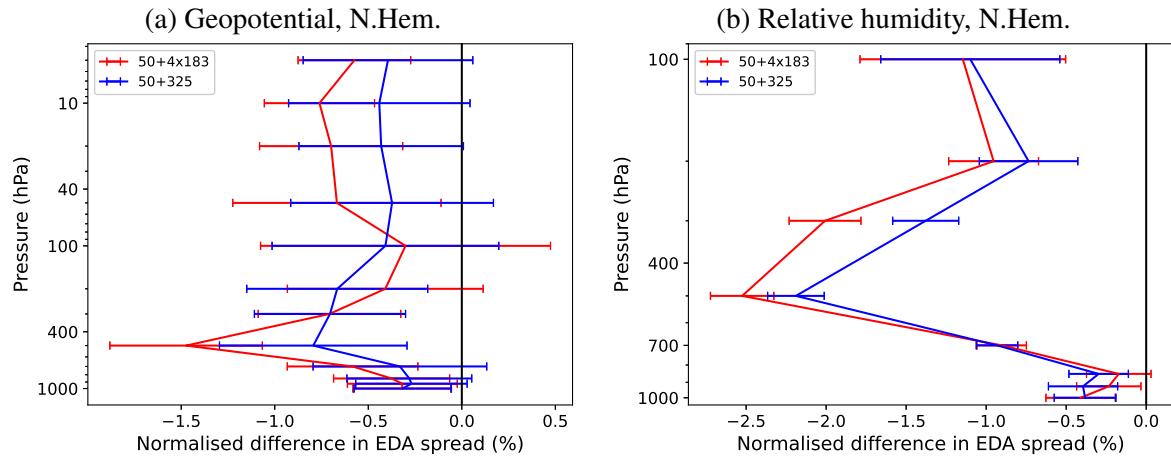
Figure 15: As Fig. 14a but for the geopotential height (a) and tropospheric relative humidity (b) over the Northern Hemisphere.

impact of the 325 GHz channels. However, the influence of this is probably relatively small, as the differences in the assumed noise values are not large and the instrument noise is considered a comparatively small contribution of the overall observation error for these channels which tends to be dominated by representation error.

The above findings suggest clear positive impact from the 325 GHz channels when added to the 50-GHz temperature-sounding channels as the only set of humidity-sounding channels. This is an important result, as it demonstrates, for the first time, the benefit of these channels in a global NWP framework. It also suggests that the chosen assimilation approach is sound and adequate for exploiting the information contained in these channels on their own.

6 Combining 50, 183 and 325 GHz channels

We will now investigate adding the 325 GHz channels on top of the 50 and 183 GHz sounding channels, with the aim of evaluating the combined impact from these three sounding bands. To do so, we perform two further EDA experiments, again using the simulated six-satellite nominal EPS-Sterna constellation on top of the Baseline observing system of real observations that is described in detail in Lean et al. (2023):

50+183: Experiment with the Baseline real observing system plus the 50 GHz temperature-sounding channels and the 183 GHz humidity-sounding channels from the 6-satellite nominal EPS-Sterna constellation. This is the same experiment as the one labelled "OP3-6SAT" in Lean et al. (2023).

50+183+325: As 50+183, but with the four 325 GHz channels from EPS-Sterna added.

50+183+325infl: As 50+183+325, but with the maximum cloudy observation error assigned to the 325 GHz channels inflated by a factor 1.5, for reasons that will be explained later.

The experiments again use the same EDA configuration as described in Lean et al. (2023), that is, a 10-member EDA with a spatial resolution of $T_{CO}399$ (≈ 25 km). They were run for the period 1-28 July 2019.

(a) Relative humidity, N.Hem.
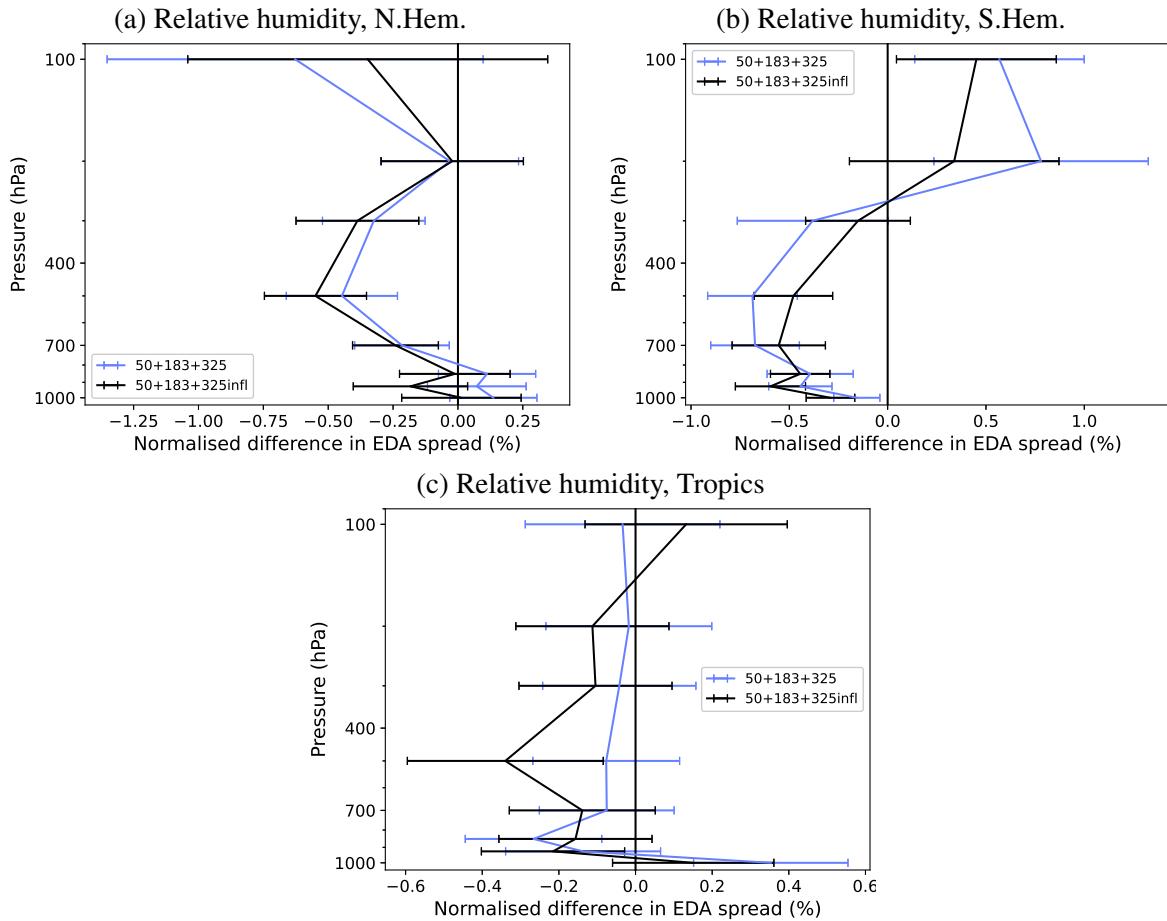
(b) Relative humidity, S.Hem.

(c) Relative humidity, Tropics

Figure 16: Vertical profiles of the EDA spread reduction for the tropospheric relative humidity in the (a) Northern Hemisphere (lat > 20°N), (b) Southern Hemisphere (lat > 20°S), and (c) the Tropics (lat < ±20°N) for the 50+183+325 experiment (blue) and the 50+183+325infl experiment (black) relative to the 50+183 experiment. Reductions in spread indicate benefit from the addition of the 325 GHz channels compared to the experiment in which only 50 and 183 GHz channels are used. Data are for the period 8-28 July 2019. Horizontal bars indicate 95 % significance intervals.

Figure 16 suggests that there is considerable benefit for relative humidity in the troposphere resulting from the addition of the 325 GHz channels. Comparisons between the 50+183+325 and the 50+183 experiments show that EDA spread reductions reach or exceed 0.5 % for the mid-troposphere over the extra-tropics, whereas over the Tropics the impact is more neutral (see the blue line in Fig. 16). The improvement in relatively humidity is likely at least partially the result of the enhanced ability to discriminate better between (ice) clouds and humidity when the 183 and 325 GHz channels are used together, due to the different sensitivities to ice clouds. This helps to resolve ambiguities in the departure signals, therefore helping the assimilation system to make increments in the appropriate fields.

For geophysical variables other than humidity, the impact of adding the 325 GHz channels in these experiments is, however, mostly neutral, with a slight degradation for wind (and to lesser extent temperature) in the Tropics (e.g., blue line in Fig. 17). For the extra-tropics, the EDA spread changes between the 50+183 and 50+183+325 experiments are not statistically significant for temperature, geopotential or wind (e.g., Fig. 17a, b). The small increase in spread for wind reaches 0.5 % in the tropical mid-troposphere and a little less in the upper stratosphere (Fig. 17c). Unexpected degradation from adding
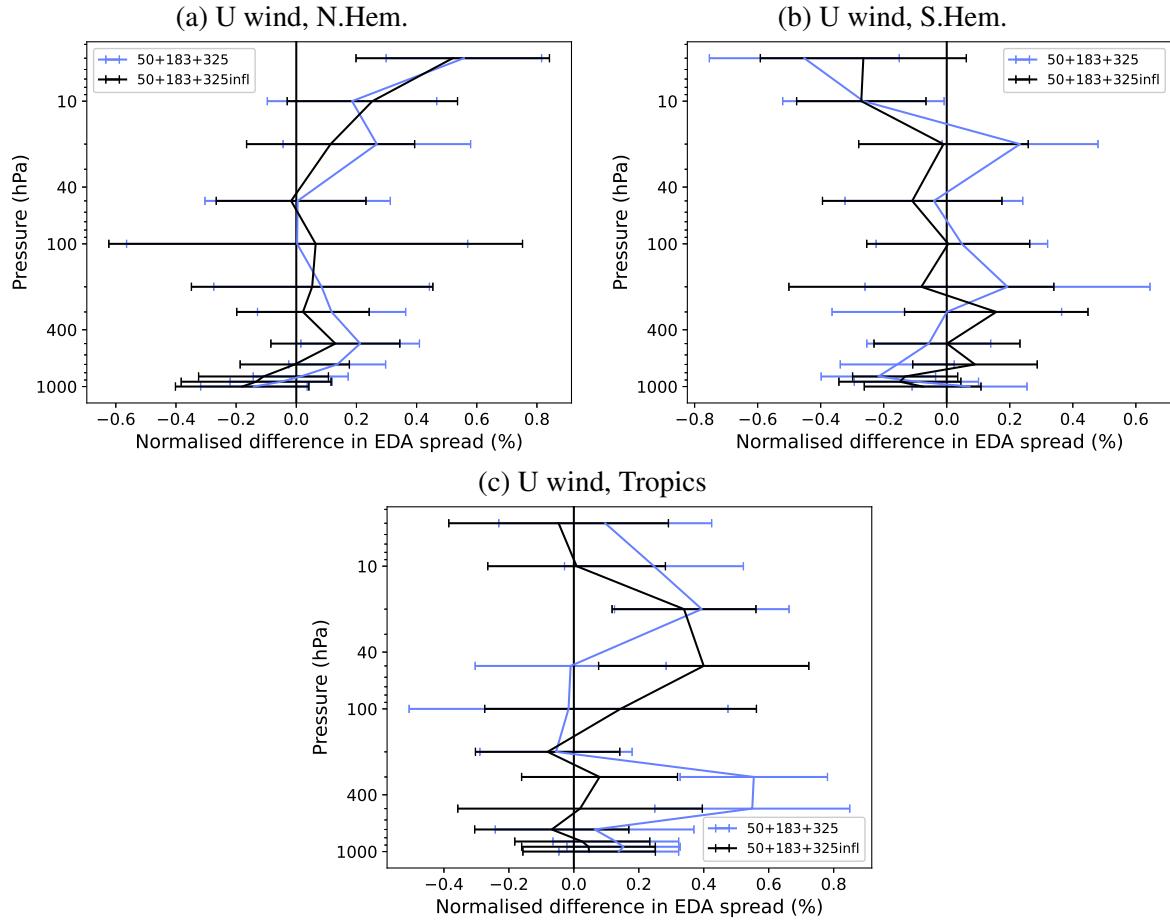
Figure 17: As Fig. 16, but for the zonal wind component.

new observations is typically the result of over-weighting the observations in the assimilation, as a result of approximations made in the assignment of the observation errors.

A plausible reason for over-weighting in our case is that we neglect the presence of inter-channel correlations in the representation error in these experiments. Such inter-channel error correlations have been found particularly relevant for humidity-sounding channels in the infrared, resulting from the finer spatial scales of the measured quantities as well as the residual influence of clouds (e.g., Bormann et al., 2010). Accounting for inter-channel observational error correlation during the assimilation has been a key advancement to allow a more extensive use of humidity-sounding channels from the water-vapour bands of the hyperspectral IR instruments (e.g., Salonen and McNally, 2019; Bormann et al., 2016; Weston et al., 2014; Hilton et al., 2009). To further support this explanation, Fig. 18 shows diagnostics of inter-channel observation error correlations obtained using the Desroziers et al. (2005) diagnostic on the control member of the EDA for clear and cloudy situations. Under the assumption that the weights assigned in the assimilation system are consistent with the true weights, the Desroziers diagnostic provides a consistency diagnostic for the observation errors, based on statistics of background and analysis departures. While the strict applicability of the diagnostic in the present experimentation may be debatable, the diagnostic shows clear blocks of inter-channel error correlations for the humidity-sounding channels (11-19). In particular, higher correlations are present between neighbouring channels as well as the respective corresponding 183 and 325 GHz channels. The correlations are particularly strong for the cloudy scenes (Fig. 18b). The diagnostics shown are in line with those typically seen for real data

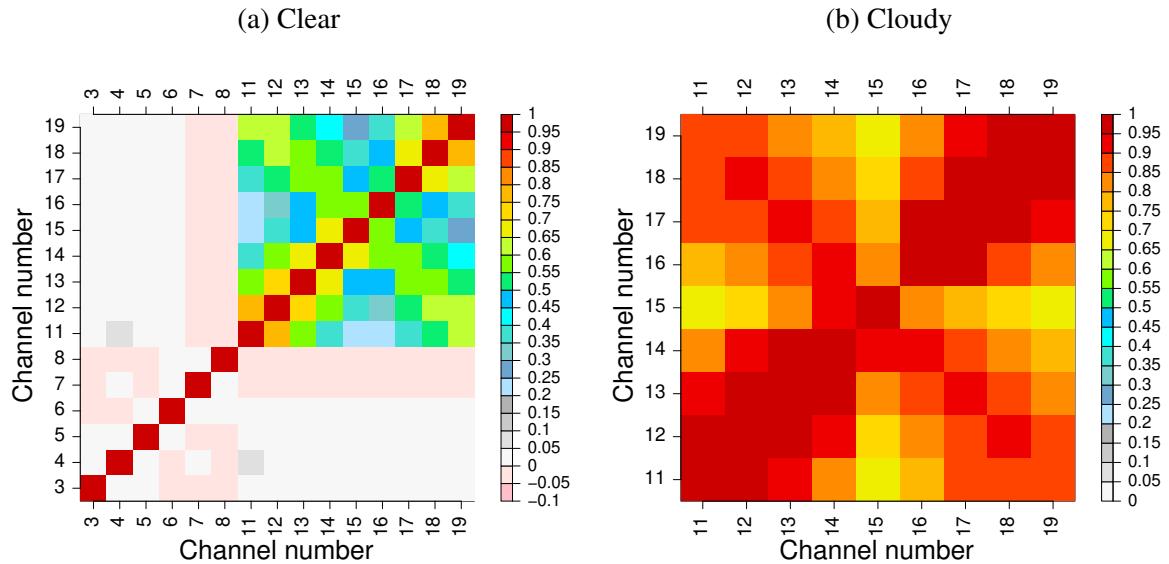(a) Clear   (b) Cloudy

Figure 18: Inter-channel error correlations derived via the Desroziers diagnostic for (a) all EPS-Sterna sounding channels used in the present study derived from clear scenes (ie with $C_{sym}^{89-165.5} < 5$ K) and (b) the 183 and 325 GHz frequencies for strongly cloudy situations only (data with $C_{sym}^{89-165.5} > 25$ K). Statistics are based on data from 2-28 July 2019, using the EDA control experiment.

(Bormann and Bauer, 2010; Bormann et al., 2013). As our assimilation assumes diagonal observation errors, such error correlations are not taken into account, and this aspect is clearly more severe when more of the humidity-sounding channels are used.

Taking inter-channel error correlations into account during the all-sky assimilation of MW radiances is an active area of research at ECMWF and elsewhere, including, for instance, ways to appropriately specify these error correlations. In addition, for the ECMWF system it is currently technically not possible to account for inter-channel error correlations at the same time as using Variational Quality Control (VarQC, Andersson and Järvinen, 1998). The latter is considered an important aspect of the all-sky assimilation of MW radiances adopted here. Developments are under-way to address this, but unfortunately they are not yet available for the present study.

As a pragmatic alternative, inflation of diagonal observation errors is often used when error correlations are present, but not accounted for in the assimilation. While not as good as taking the error correlations into account, it helps to avoid the down-sides of over-fitting the observations (e.g., Bormann et al., 2016). We therefore conducted another EDA experiment, referred to as 50+183+325infl, in which the maximum cloudy observation errors from Table 3 assigned to the 325 GHz channels were scaled by 1.5. Only the cloudy errors are scaled here, as they are most affected. The choice of the factor is somewhat ad-hoc, but leads to inflations that are in line with inflation factors typically used in the literature (e.g., Bormann et al., 2016; Eresmaa et al., 2017). It could be argued that inflation should be applied to both sets of humidity sounding channels, but this was not pursued here for reasons of simplicity.

The observation-error inflation helps to address the degradation previously seen in the tropical troposphere, as can be seen from the black line in Fig. 17c. The addition of the 325 GHz channels to the 50 and 183-GHz channels now results in no statistically significant change here. However, the small increase in spread in the stratosphere now has a somewhat larger vertical extent, possibly linked to a
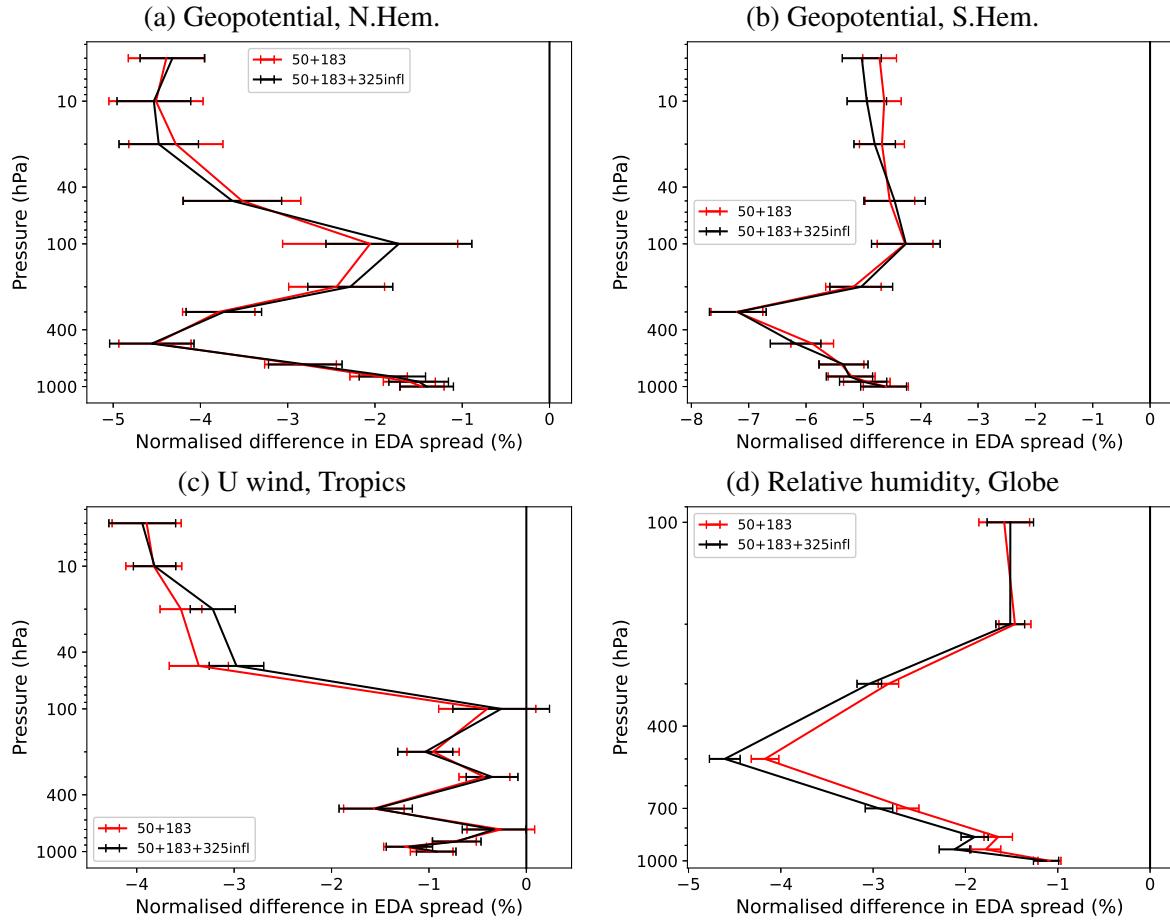
Figure 19: Vertical profiles of the EDA spread reduction for the 50+183 (red) and the 50+183+325infl (black) experiments, relative to the Baseline experiment with no EPS-Sterna data. The different panels show results for the the geopotential over the (a) Northern Hemisphere (lat > 20°N) and (b) Southern Hemisphere (lat > 20°S), as well as (c) zonal wind in the Tropics (lat < ±20°N) and (d) relative humidity in the troposphere over the full globe. Reductions in spread indicate benefit from the addition of EPS-Sterna to the Baseline observing system. Data are for the period 8-28 July 2019. Horizontal bars indicate 95 % significance intervals.

poor handling of gravity waves triggered by convection in this region. For other regions and variables, comparisons between the experiments 50+183+325infl and 50+183+325 show no statistically significant change from the introduced error inflation (e.g., Figures 16 and 17a, b). Overall, the results confirm some sensitivity to the setting of observation errors, and it is expected that further benefit could be achieved from the combined use of the two sets of humidity-sounding channels when inter-channel observation error correlations can be better taken into account.

To further assess the additional impact of the 325 GHz channels, other aspects have also been examined, including maps of the EDA spread reduction resulting from the addition of these observations. The changes are, however, relatively small and noisy, with no clear signal of more localised stronger impact in certain geographical regions (not shown). A longer experimentation period may be needed to further assess this aspect.

For completeness, Fig. 19 shows the overall impact from adding the full sounding capabilities of EPS-

Sterna to the Baseline observing system of existing observations. The Figure includes the EDA spread reductions from the 50+183+325infl experiment with overall the best performance together with those for the 50+183 experiment previously shown in Lean et al. (2023). As discussed in detail in Lean et al. (2023), the addition of EPS-Sterna results in a very significant reduction of the EDA spread, suggesting sizeable benefits in forecast impact from these new observations. The benefit that can currently be demonstrated from the 325 GHz channels is comparatively small (compare black and red lines), but nevertheless statistically significant for relative humidity.

7 Summary and conclusions

In the present study, we have developed a strategy to simulate and assimilate the new 325 GHz channels available from the EPS-Sterna constellation, and we have evaluated their expected impact using the EDA technique. As there is no experience with these channels from heritage instruments, they were previously not included in the evaluation of the potential future impact of the EPS-Sterna constellation presented in Lean et al. (2023). The simulation and assimilation is performed in an all-sky context, adopting the latest developments in scattering radiative transfer, particularly tailored to the use of sub-mm channels in connection with ice clouds (Geer et al., 2021). Ocean-surface emissivity modelling has been done using FASTEM-6 (Kazumori and English, 2015). While FASTEM-6 has not been developed for the use with sub-mm channels, comparisons with the more applicable SURFEM model suggest an adequate performance, at least for geographical areas that are not screened out by quality control. A comparison of weighting functions has allowed each 325 GHz channel to be matched with a traditional 183 GHz of similar vertical sensitivity to the atmosphere (Eriksson et al., 2020). The brightness temperature simulations show good agreement between matched channels in clear-sky areas, whereas areas with ice clouds show larger brightness temperature depressions at 325 GHz, as expected from the greater sensitivity to ice scattering (Eriksson et al., 2020). Geophysical quality control choices for the 325 GHz channels have been adopted from the corresponding 183 GHz channels in our EDA experimentation.

A key development in the present work was the formulation of an observation-error model tailored to the 325 GHz channels. The model adopts the standard approach of the all-sky observation error model, but uses a new cloud indicator, $C_{sym}^{325\pm6.6}$, which incorporates information from the stronger ice scattering in the lowest peaking 325 GHz channels. The new indicator is based on comparing observed or modelled all-sky brightness temperatures with clear-sky simulations from the model background. The indicator is used in the observation error model to assign larger observation errors in cloudy regions, reflecting larger representation error. Observation error correlations are neglected and only diagonal errors are assigned. With the new cloud indicator employed in the observation error model, PDFs of normalised background departures (ie O-B normalised by the assigned observation error) are more Gaussian than with an observation-error model that uses a scattering index derived from the 89 and 165 GHz channels as cloud indicator instead. The latter cloud indicator is presently used for the 183 GHz channels in the ECMWF system. This suggests that the new cloud indicator captures better the situation-dependence of the representation error of the 325 GHz channels. Use of $C_{sym}^{325\pm6.6}$ may also be beneficial for the 183 GHz channels to improve the Gaussianity of the normalised background departures, but this is left as future work.

When the 325 GHz channels are used instead of the 183 GHz channels, the EDA experiments indicate an impact from the four 325 GHz channels that is broadly similar to that from the assimilation of the four matched 183 GHz channels. This is a key result of the present study, as it demonstrates for the first time the usefulness of these channels for global NWP. The result also highlights that our assimilation setup is adequate to extract this information when they are added as the only set of humidity-channels from EPS-

Sterna. For relative humidity, the benefit from 325 GHz is slightly reduced relative to 183 GHz. This different behaviour could be linked to the higher sensitivity to ice scattering in the 325 GHz channels, which may impair the amount of information obtained from water vapour signals when these channels are used as the only humidity-sounding channels.

When added on top of the 50 and 183 GHz channels available from EPS-Sterna, some benefits are found for relative humidity compared to using the 50 and 183 GHz channels only, but otherwise results are largely neutral. Note that this impact is in addition to the very significant benefit previously shown just with the 50 and 183 GHz channels (Lean et al., 2023). Additional experiments highlight some sensitivity to the assignment of the observation errors, and an increase in the observation error assigned for cloudy regions is required to avoid a small degradation for wind forecasts in the tropics. A possible explanation for this finding is that the 325 GHz channels are otherwise over-weighted due to the presence of observation error correlations that are currently neglected in the observation error model. Consistent with this explanation, strong inter-channel error correlations were diagnosed from the experiments performed in this study, particularly between the corresponding 325 and 183 GHz channels. These are thought to be the result of similar representation error for these channels peaking at similar altitudes. Note that representation error is a function of the atmospheric state and cannot be reduced through adding further observations, but instead needs to be taken into account during the assimilation. In this context it is worth noting that the correlations in the representation error may have been smaller if the 325 GHz channels had been chosen in such a way that their weighting functions peak between those of the 183 GHz channels, rather than at similar altitudes. This would have also benefited the vertical resolution for humidity that should be obtainable from EPS-Sterna in an assimilation system, albeit possibly at the expense of a less clean identification of ice-cloud signals.

Developments towards accounting for inter-channel error correlations in the all-sky assimilation of MW radiances are currently under way at ECMWF, and these may lead to further benefit from the use of the 325 GHz channels. Accounting for inter-channel error correlations has been a key development to obtain impact from a larger selection of humidity-sounding channels from hyperspectral IR instruments, for which the addition of further humidity channels previously led to a degraded impact (Salonen and McNally, 2019; Hilton et al., 2009).

The experience with the assimilation of the 325 GHz channels is a reminder that EDA evaluations necessarily reflect the maturity of the use of the observations at the present time. Developments in the assimilation system and the use of the relevant observations affect the impact that is achieved from a given set of observations, and the impact that is realised when the actual observations become available will reflect this. In turn, in the present study, the EDA experiments have allowed a first indication of what might be relevant preparatory and development activities, some of which can also be performed prior to launch.

The present study has also highlighted other areas of potential future work. Aside from accounting for observation error correlations, the modelling of the observation errors could be further revised, including whether the better characterisation of ice clouds in the new 325 GHz-based cloud indicator brings benefits to the assimilation of the 183 GHz humidity-sounding channels. With real data available from AWS soon, some aspects of the forward-simulation of the brightness temperatures should also be revisited. For instance, in our study we use a single type of ice particles in the RTTOV-SCATT simulations. While this simplification has proven adequate for currently used frequencies in the ECMWF system (Geer, 2021), it needs to be re-evaluated with real data for the sub-mm frequencies with much larger sensitivity to ice clouds. Similarly, the adequacy of FASTEM-6 or SURFEM to model frequencies up to 325 GHz should be confirmed with real data.

The assimilation of the 325 GHz channels may also benefit from wider enhancements of the ECMWF assimilation system that are currently under development. One aspect of note is the the addition of clouds in the control variable, prompted by the increasing use of cloud-affected observations from satellites. In the current ECMWF system, cloud fields are not part of the control variable. This means the analysis can respond to cloud signals in the observations only by adjusting other variables describing humidity, temperature or wind, which then affect the model cloud fields via the integration of the forecast model over the assimilation window in 4D-Var. For the observations currently assimilated through the all-sky approach, this has not been found to be a major limitation, as time-scales of clouds are typically just a few hours and their evolution is hence dominated by other atmospheric variables that are part of the 4D-Var control variable. However, some ice-clouds can show longer time-scales, and without a cloud control variable 4D-Var may be unable to produce the correct increments in these cases, at least for the first few hours of the assimilation window. The development of the new cloud control variable may hence be of particular benefit for EPS-Sterna, as it is expected to allow a better separation of cloud and humidity signals in the early part of the assimilation window when both sets of humidity-sounding channels are present. In this context, the effect of EPS-Sterna on the cloud analysis should be investigated further, as an improved characterisation of clouds is one of the motivations for including the 325 GHz channels for the EPS-Sterna instrument.

Acknowledgements

Appendix A   Estimation of clear-sky observation errors

In the following, the method to derive minimum assigned clear-sky observation error values from given NEDT values is presented. This has been developed in a previous study, and the text is reproduced here from Lean et al. (2022b) for convenience.

Observation errors assigned in data assimilation describe different sources of error, typically classified into measurement error (such as instrument noise) and representation error. To devise the parameters for the observation error model discussed in section 4, we assume that the representation error for the new data is the same as for the real data, but only the instrument noise is different. This is justified, given the similarity of the channels as well as the similarity of the footprint sizes. Note, however, that for real data we currently do not explicitly model the contributions from instrument noise and representation error separately in the observation error model. Instead, the parameters of the observation error model are set empirically, based on the standard deviation of background departures which provide an upper limit for the overall observation error in the absence of correlations between observation and background error. In order to separate out the contribution from instrument noise some reverse engineering is needed. The instrument noise only matters for the clear-sky parameter of the error model, as otherwise representation error dominates, so the following focusses only on the clear-sky parameter. For the cloudy observation error setting, we simply adopt the same values as used for real data, as sample NEDT is a negligible contribution.
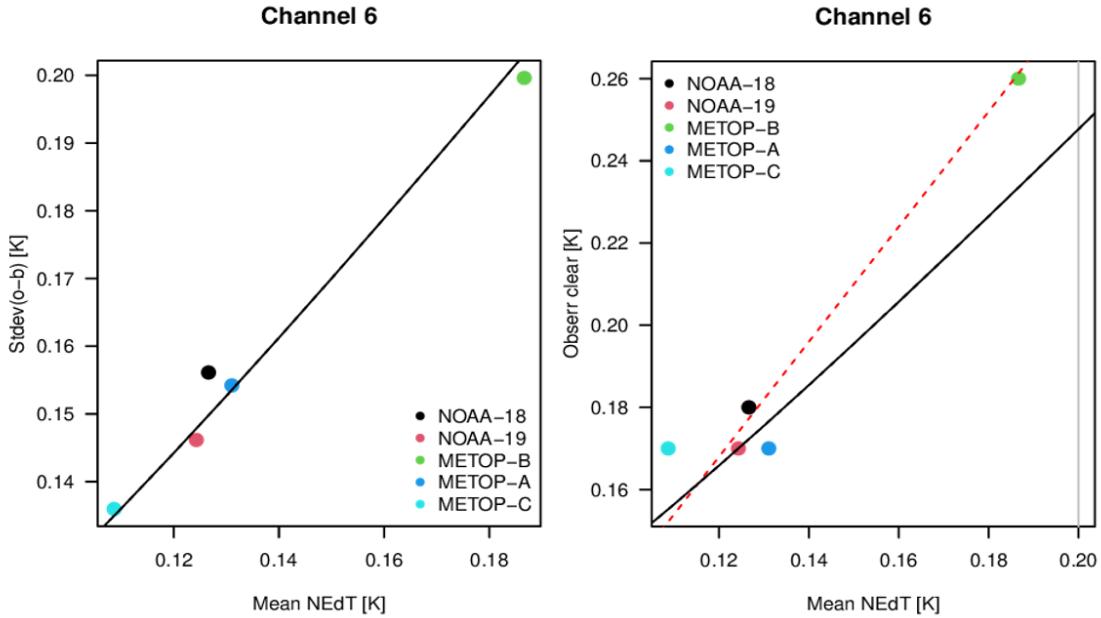
Figure 20: Standard deviation of O-B vs. sample NEDT (left) and assigned clear sky observation errors vs. sample NEDT (right) for AMSU-A channel 6 on various satellite platforms. Fitted lines show the results from using a simple scaling of sample NEDT (red dashed) or using equation 5 (solid black line).

To link the empirically assigned clear-sky observation error to the sample NEDT, we proceed as follows: we model our assigned (clear-sky) observation error $\sigma_{o,clr}$ as a combination of the instrument noise σ_{NEDT} and representation error σ_r, and a scaling factor a which accounts for other neglected effects in the error modelling, such as error correlations. Assuming that the two error contributions are uncorrelated, the relationship becomes:

$$\sigma_{o,clr} = a\sqrt{\sigma_{NEDT}^2 + \sigma_r^2} \tag{5}$$

The values for σ_r and a are derived from real data as follows: First, σ_r is derived by considering standard deviations of background departures and channel-specific sample NEDT values provided with the data. This makes use of the fact that we presently have several instruments available in the ECMWF system, with some variations in the instrument noise performance. For the temperature sounding channels, there is mostly a clear relationship reflecting that instrument noise is a dominant part of the error budget (e.g. Fig. 20, left). The relationship follows $\sqrt{\sigma_{NEDT}^2 + \sigma_r^2}$, with an appropriately fitted σ_r. Then, the scaling factor a is derived by considering assigned σ_o and sample NEDT values for real data. The relationship between these two quantities is not as clear (e.g. Fig. 20, right). This is primarily because instrument noise values have changed since the parameters of the observation error model have been derived some time ago, and the parameters have not been updated. The value a is chosen to nevertheless give the best overall fit, using the relationship given in equation 5 with σ_r derived previously. Separate parameters have been derived for land and sea, and the values are given in Table 4.

For the temperature sounding channels, the representation error derived in this way is typically relatively small, with values mostly around 0.1 K and hence smaller than the sample NEDT. In contrast, representation errors for the humidity sounding channels are much larger, with values of 1.4-2.0 K and hence larger than the instrument noise. This reflects that representation error plays a much larger role for these channels, even in clear-sky regions. In fact, the observation error assignment for humidity sounding channels

Table 4: Parameters used to derive the clear-sky observation error values from the sample NEDT values for each channel, in terms of the scaling factor a and the representation error σ_r. Values were derived using departure statistics from the ECMWF system over two seasons (13-31 May and 12-31 Oct 2021), as described in the main text.

AMSU-A/MHS channel	a	σ_r	a	σ_r
	sea		land	
AMSU-A 5	1.15	0.14	1.15	0.24
AMSU-A 6	1.15	0.08	1.15	0.13
AMSU-A 7	1.15	0.08	1.15	0.08
AMSU-A 8	1.15	0.08	1.15	0.08
AMSU-A 9	1.15	0.09	1.15	0.09
MHS 3	1.30	1.4	1.3	1.45
MHS 4	1.25	1.5	1.3	1.35
MHS 5	1.10	1.95	1.4	1.4

in the ECMWF system currently neglects different instrument noise values for different instruments, and instead assigns the same value. The scaling factors a tend to be similar for different temperature sounding channels, with values of around 1.15, whereas they tend to be slightly larger for the humidity sounding channels, with values up to 1.4.

The above derived relationships are used with the sample NEDT estimates for the EPS-Sterna instrument (divided by three to account for the 3x3 averaging) to obtain the clear-sky observation error values for the small satellite data. The resulting values for the temperature sounding channels are around 0.25-0.28K, which is slightly higher than AMSU-A equivalents. For the humidity sounding channels, the resulting values are very similar to those used for MHS. While primarily derived for the purpose of specifying observation error values for the present study, the derived relationships could also be considered in a refined observation error model in the ECMWF system that allows for changes in the NEDT of real data, as a result of instrument ageing and other effects.

Appendix B   Alternative cloud indicator investigations

In this part we will summarise further investigations regarding alternative cloud indicators used in the observation error model for the 325 GHz channels. One candidate cloud indicator considered is a variant of the scatter index $C_{sym}^{89-165.5}$, with the 89 GHz and 165.5 GHz channels substituted for 178.811 GHz and 325 ± 6.6 GHz in equations 1 and 2, respectively:

$$C_{land}^{178.811-325\pm6.6} = BT_{178.811} - BT_{325\pm6.6} \tag{6}$$

$$C_{ocean}^{178.811-325\pm6.6} = (BT_{178.811} - BT_{325\pm6.6}) - (BT_{178.811}^{clr} - BT_{325\pm6.6}^{clr}) \tag{7}$$

Similar to $C_{sym}^{89-165.5}$, this cloud indicator makes use of the different cloud scattering signatures between the two channels, while in clear-sky regions the two channels show very similar values. The scattering signatures are, however, strongly dependent on the density of the ice particles: For low-density snow/ice particles, the BT monotonically decreases from 183 GHz to 325 GHz (e.g., Fig. 9 in Geer et al., 2021). This depression is also greater than that between the 89 and 165.5 GHz channels and therefore helps to better identify ice cloud signals. In contrast, for denser particles, at higher frequencies the trend in BT can reverse, i.e. BT can increase with increasing frequency. In cloud situations with denser particles, this can lead to a reduced BT difference at between 183 and 325 GHz, and this would be interpreted as a weaker cloud presence. For the densest particles, the reversal could even result in a negative difference, erroneously suggesting that there is no cloud.

To avoid the down-sides of $C_{sym}^{178.811-325\pm6.6}$ for denser particles, we consider another cloud indicator, that takes the maximum value between $C_{sym}^{89-165.5}$ and $C_{sym}^{178.811-325\pm6.6}$:

$$C_{sym}^{max} = max[C_{sym}^{89-165.5}, C_{sym}^{178.811-325\pm6.6}] \tag{8}$$

This cloud indicator is aimed at combining the power of identifying scattering signals of both of the separate indicators. Note that a scatter index formed by 89-325±6.6 GHz was also explored as a potential basis for a cloud indicator (not shown). While also suffering from the same issues of potentially reduced/negative scattering index values, other undesirable features arising from e.g. a more extreme difference in sensitivity to hydrometeors and water vapour or the mismatch in weighting functions led to a poorer suitability than the frequency difference proposed above.

It is worth noting that for the simulations considered here, the radiative transfer model assumes a fixed ice particle and therefore we will not capture the more variable behaviour expected for different ice particles discussed above. Until being able to analyse real MW data, it is difficult to predict the impact of this issue and in particular, how often with real observations we would encounter cases associated with the denser ice particles that could reduce the effectiveness of a 183-325 GHz based scatter index.

Figure 21 illustrates the typical geographical variability of the two cloud indicators. Both indicators identify areas of increased ice scattering through higher values, with $C_{sym}^{178.811-325\pm6.6}$ particularly picking out ice clouds around the frontal features over the extra-tropics, with similar features as $C_{sym}^{325\pm6.6}$ shown in Fig. 4. Over land there are large areas of negative values in $C_{sym}^{89-165.5}$ which are close to zero in $C_{sym}^{178.811-325\pm6.6}$. Closer agreement of BT in the absence of ice clouds results in $C_{sym}^{178.811-325\pm6.6}$ closer to zero in many areas, a result of the similar weighting functions of the two channels used.
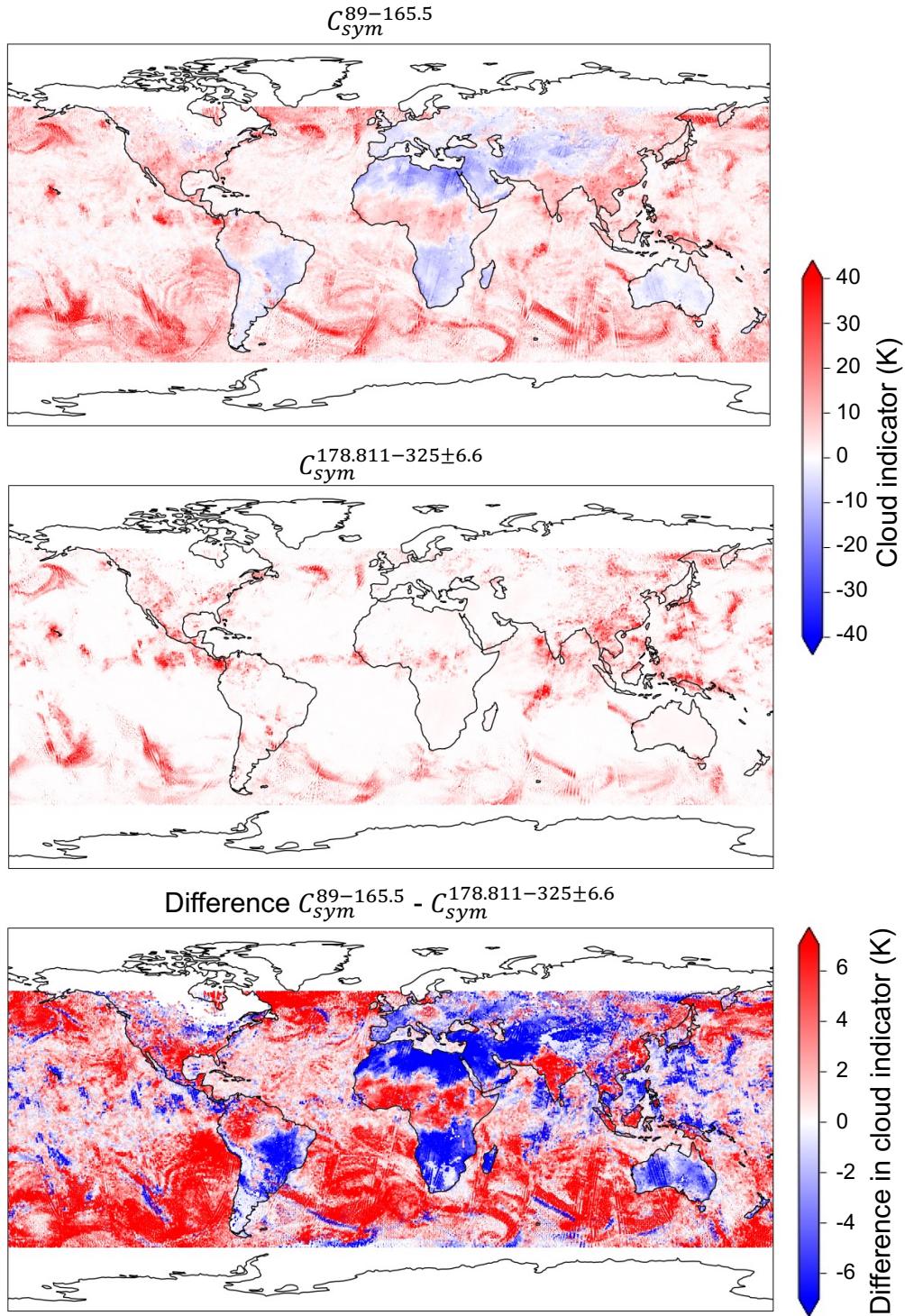
Figure 21: Map showing $C_{sym}^{89-165.5}$ (top) and $C_{sym}^{178.811-325\pm6.6}$ (middle). The lower panel displays the difference between the two cloud indicators where blue colours correspond to higher values in $C_{sym}^{178.811-325\pm6.6}$. Data are for the period 17-23 July 2019 for one EPS-Sterna satellite where no screening has been applied apart from latitude limits at $\pm60°$N.
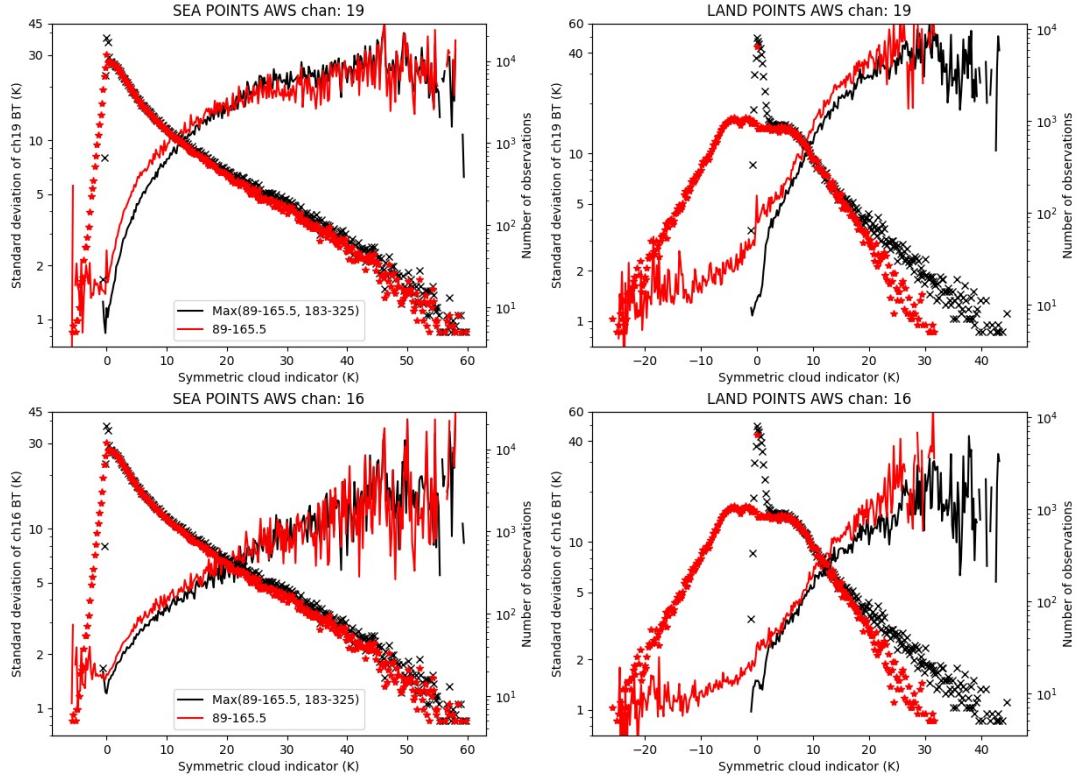
Figure 22: Standard deviation of O-B for the 325±6.6 channel (top row) and the 325±1.0 GHz channel (bottom row) binned as a function of the symmetric cloud indicator $C_{sym}^{89-165.5}$ (red line) or C_{sym}^{max} (black line). Crosses in the same corresponding colours indicate the number of observations in each bin (right y-axis). Data are for all observations not yet subject to quality control from an EPS-Sterna satellite for a period of seven days over ocean only (left panel) and land only (right panel), limited to ±60°N to exclude sea ice contamination.

Figure 22 illustrates the behaviour of the standard deviation of O-B as a function of $C_{sym}^{89-165.5}$ and C_{sym}^{max} for the lowest and the highest peaking 325 GHz channels. The standard deviation of O-B generally rises smoothly up to a plateau for larger cloud indicator values, as expected. When using C_{sym}^{max} (black line), the

Table 5: Minimum clear-sky and maximum cloudy observation errors used in the C_{sym}^{max}-based all-sky error model for the 325 GHz channels. The value of C_{sym} that defines the saturated cloud presence is also given. For all channels, the minimum value of C_{sym}, indicating clear-sky, is zero.

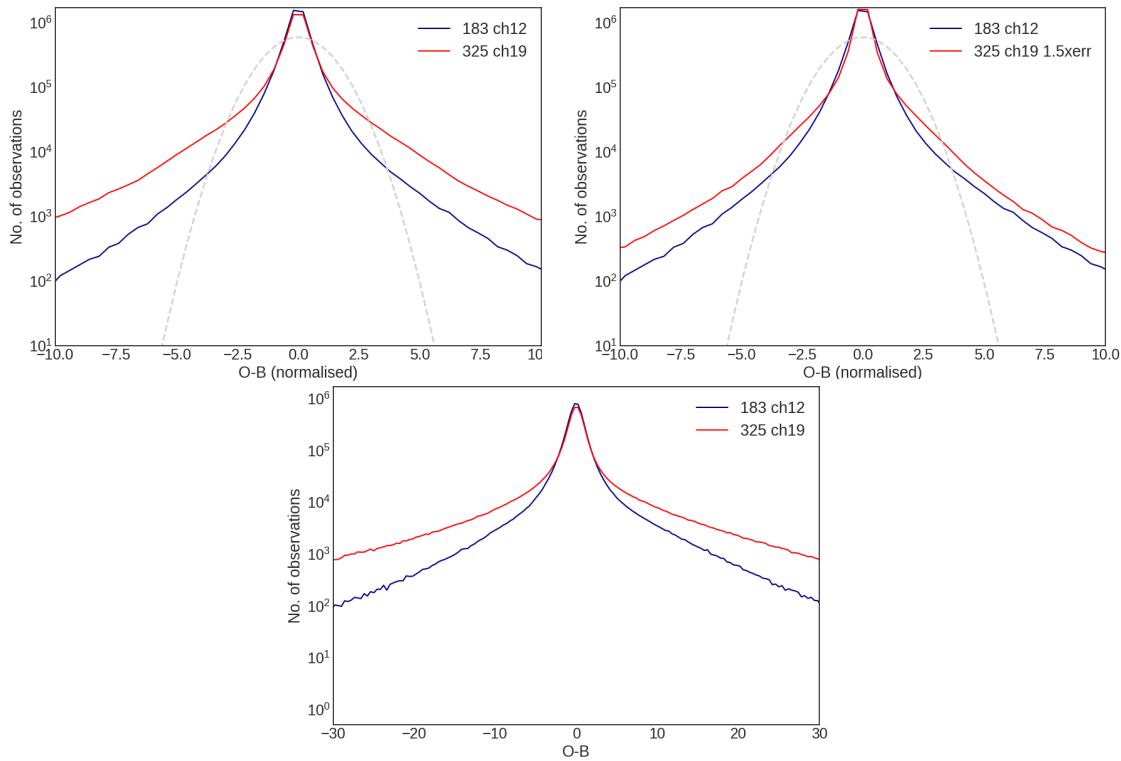| Channel number	C_{sym} upper limit		Min clear error		Max cloudy error	
	Sea	Land	Sea	Land	Sea	Land
16	37	20	1.9	2	17.6	10.4
17	34	21.5	2	1.9	24.2	17.5
18	34	21.5	2.1	1.9	26.5	22.2
19	34	21.5	2.1	1.9	31.7	26

Figure 23: Probability density functions of the background departure normalised by the observation errors (top row) for the 325±6.6 channel (red) and the 178.811 GHz channel (blue). The observation error model employs the $C_{sym}^{89-165.5}$ and the C_{sym}^{max} cloud indicator for the 178.811 GHz channel and the 325±6.6 channel, respectively. Values for the observation error model are defined as given by Tables 3 and 5 (top left), and with all minimum and maximum values of observation error inflated by a factor of 1.5 for the 325 GHz channel only (top right). An example Gaussian curve (with standard deviation of 2) has been added to demonstrate the appearance of a perfect Gaussian shape. The bottom panel shows the PDF of the background departures prior to normalisation. Data are for the northern hemisphere (lat > 20°N) for a period of 10 days 8-18 July 2019 before quality control, taken from the control member of an EDA experiment (i.e. observations are unperturbed).

overall dependence changes relatively little, as the value of C_{sym}^{max} is predominantly the same as $C_{sym}^{89-165.5}$, except for the areas with the largest effect from ice clouds (cf Fig. 21). As a result, there is a slightly higher number of observations with larger cloud indicator values for C_{sym}^{max} compared to $C_{sym}^{178.811-325\pm6.6}$, as well as a slight shift in the standard deviation of O-B towards smaller values for smaller cloud indicator values. This suggests that $C_{sym}^{178.811-325\pm6.6}$ is indeed slightly better able to distinguish between situations of low and high standard deviations, but the effect is relatively small.

Fig. 23 (top, left) examines to what extent histograms of background departures normalised by the assigned observation error follow a Gaussian distribution. As discussed in section 4.4, the all-sky observation error model plays an important role in transforming the highly non-Gaussian distribution of the actual background departures into one that is more Gaussian when normalised departures are considered. Here, the observation error model for the 183 GHz channel employs the $C_{sym}^{89-165.5}$ cloud indicator as usual, whereas the 325 GHz channels use the observation error model based on C_{sym}^{max}. As can be seen, the 325 GHz channel shows considerably stronger tails than the 183 GHz counterpart, as well as a
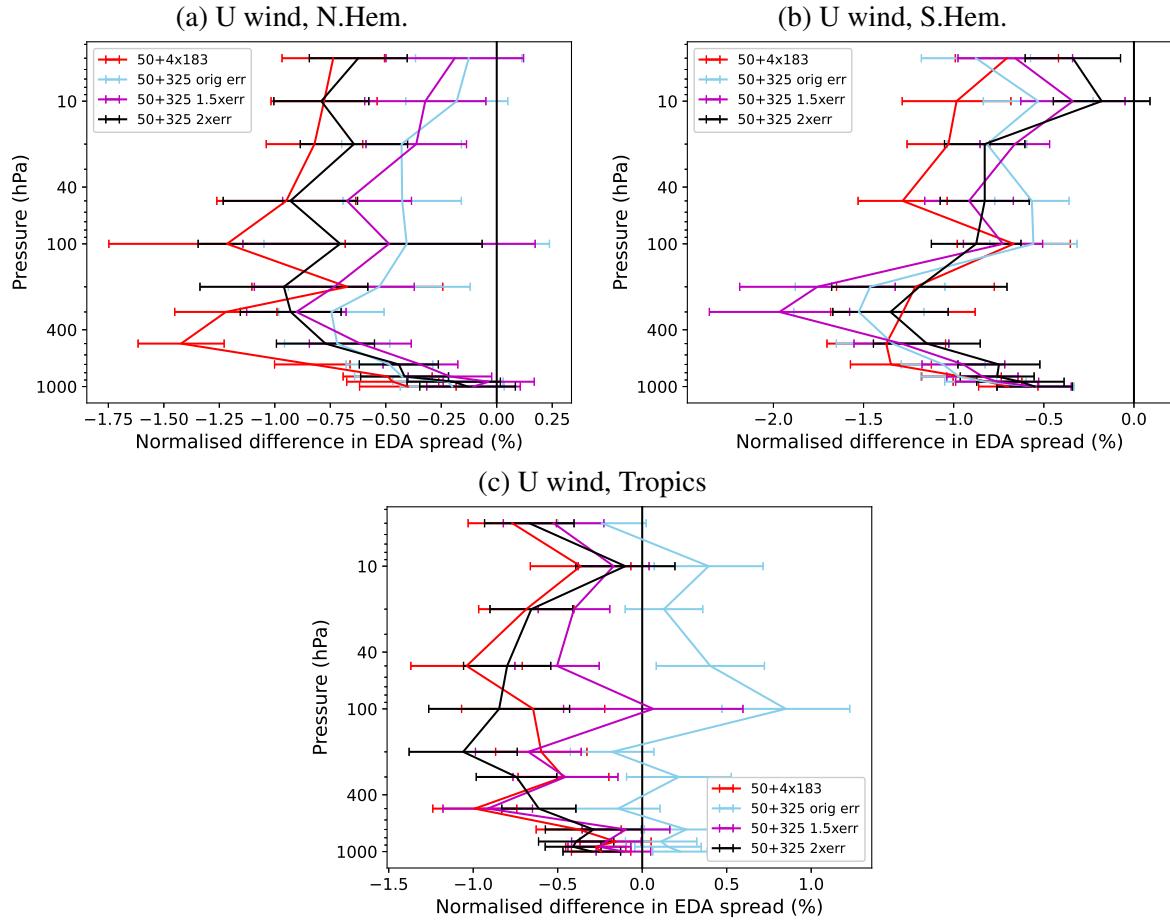
Figure 24: Vertical profiles of the EDA spread reduction compared to the 50only experiment for the U component of wind in the (a) Northern Hemisphere (lat > 20°N), (b) Southern Hemisphere (lat > 20°S) and (c) the Tropics (lat < ±20°N) for the 50+4x183 experiment (red) and three experiments in which the 325 GHz channels have been added to the 50only experiment instead, using the C_{sym}^{max}-based observation error model. The three experiments with 325 GHz channels use different settings for the parameters of the error model, that is, values as shown in Table 5 (blue), and values multiplied by a factor 1.5 (purple) or 2.0 (black). Reductions in spread indicate benefit from the addition of the 325 GHz channels or the top-four 183 GHz channels. Data are for the period 8-28 July 2019. Horizontal bars indicate 95 % significance intervals.

weaker maximum. For both channels, the shape of the distribution is quite far from that of a Gaussian distribution, but the situation appears to be worse for the 325 GHz channel. The non-Gaussianity of the normalised departure distribution for the 183 GHz channels has been previously noted by Geer et al. (2014) as a short-coming of the $C_{sym}^{89-165.5}$-based observation error model. Assimilation of the 183 GHz channels with this error model has nevertheless been found to perform sufficiently well.

Also shown in Fig. 23 (top, right) is the distribution of normalised departures resulting from scaling the assigned observation errors by 1.5 compared to the originally assigned values. As can be seen, this successfully reduces the tails of the distributions of the normalised background departures and brings it closer to that of the equivalent 183 GHz channel, although still with more outliers remaining. While such scaling does not improve the modelling of the situation-dependence, it helps to avoid that the observations in the tail of the distribution receive too much weight during the assimilation. Another option to
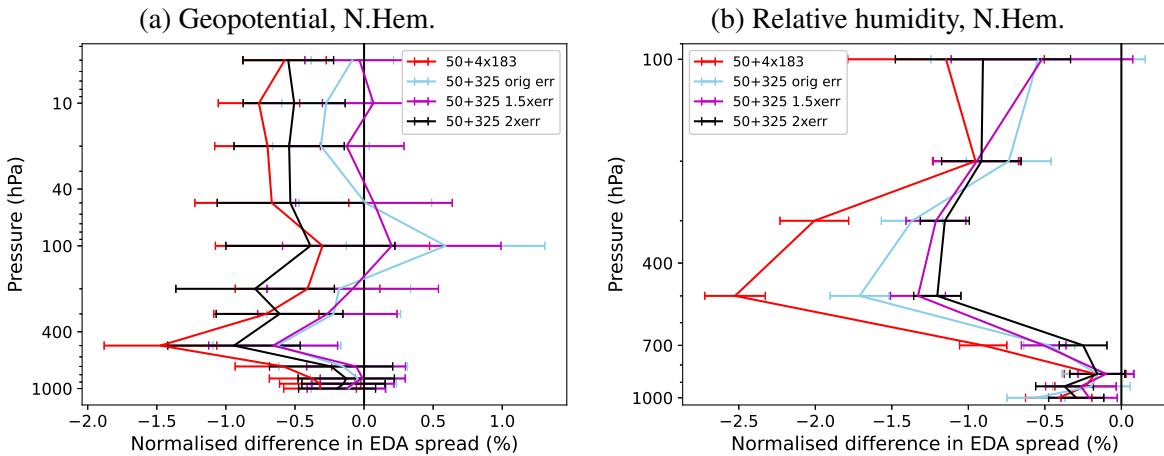
Figure 25: As Fig. 24a but for the geopotential height (a) and tropospheric relative humidity (b) in the Northern Hemisphere.

avoid over-weighting of these observations would be to revisit the settings for Variational Quality Control (VarQC, Andersson and Järvinen, 1998). This estimates the likelihood that the error for a given observation belongs to a white-noise distribution rather than a Gaussian during the assimilation and adjusts the weights assigned to the observations accordingly. However, the VarQC settings for MW humidity-channels are already quite stringent, so this was not pursued here.

EDA experiments were performed using both the un-inflated and inflated versions of the C_{sym}^{max}-based observation error model, similar to the ones presented in sections 5 and 6. They also show benefit from the assimilation of the 325 GHz channels when used instead of the 183 GHz channels, but spread reductions are overall smaller than those seen in the experiments that use the $C_{sym}^{325\pm6.6}$-based observation error model discussed in sections 5 and 6 (e.g., Figure 24 and 25, cf Figures 14 and 15, respectively). Significant inflation of the observation error is required to improve the impact, with factors of 1.5-2.0 leading to the overall best results. With such inflation applied, the EDA spread reductions are more in line with those obtained with the $C_{sym}^{325\pm6.6}$-based observation error model. When the combined channel set is used, the impact of the 325 GHz channels is overall also not as favourable as the impact of the 50 and 183 GHz channels on their own (not shown). A likely explanation of these results is that the poorer Gaussianity of the normalised departures obtained with the C_{sym}^{max}-based observation error model is indeed leading to poorer weighting of the observations in the assimilation, in particular to over-weighting of observations in the tails of the distribution, for which a larger observation error would be more appropriate. As a result of these findings, the $C_{sym}^{325\pm6.6}$-based observation error model is the preferred choice for our EDA experimentation presented in the main part of the report.

References

Andersson, E., Järvinen, H.J., 1998. Variational quality control. ECMWF Technical Memorandum 250, 31pp. doi: 10.21957/lqz2wn16g.

Bell, B., Bühler, S., Crewell, S., Eriksson, P., Geer, A., Mahfouf, J.F., Marzano, F.S., Prigent, C., Tonboe, R., 2017. MWI-ICI Science Plan. A report from the MWI-ICI Science Advisory Group. EUMETSAT Version 3.2. URL: https://www-cdn.eumetsat.int/files/2020-04/pdf_science_epssg_mwi_ici_plan.pdf.

Bormann, N., Bauer, P., 2010. Estimates of spatial and inter-channel observation error characteristics for current sounder radiances for NWP, part I: Methods and application to ATOVS data. Quart. J. Roy. Meteor. Soc. 136, 1036–1050. doi: `10.1002/qj.616`.

Bormann, N., Bonavita, M., Dragani, R., Eresmaa, R., Matricardi, M., McNally, T., 2016. Enhancing the impact of IASI observations through an updated observation-error covariance matrix. Quart. J. Roy. Meteor. Soc. 142, 1767–1780. doi: `10.1002/qj.2774`.

Bormann, N., Collard, A., Bauer, P., 2010. Estimates of spatial and inter-channel observation error characteristics for current sounder radiances for NWP, part II: Application to AIRS and IASI. Quart. J. Roy. Meteor. Soc. 136, 1051–1063. doi: `10.1002/qj.615`.

Bormann, N., Fouilloux, A., Bell, W., 2013. Evaluation and assimilation of atms data in the ecmwf system. Journal of Geophysical Research: Atmospheres 118, 12,970–12,980. doi: `10.1002/2013JD020325`.

Bormann, N., Lawrence, H., Farnan, J., 2019. Global observing system experiments in the ECMWF assimilation system. ECMWF Technical Memorandum 839. doi: `10.21957/sr184iyz`.

Desroziers, G., Berre, L., Chapnik, B., Poli, P., 2005. Diagnosis of observation, background, and analysis-error statistics in observation space. Q.J.R.Meteorol.Soc. 131, 3385–3396. doi: `10.1256/qj.05.108`.

Dinnat, E., English, S., Prigent, C., Kilic, L., Anguelova, M., Newman, S., Meissner, T., Boutin, J., Stoffelen, A., Yueh, S., Johnson, B., Weng, F., Jimenez, C., 2023. PARMIO: A Reference Quality Model for Ocean Surface Emissivity and Backscatter from the Microwave to the Infrared. Bull. Amer. Meteor. Soc. 104, E742–E748. doi: `10.1175/BAMS-D-23-0023.1`.

English, S.J., 1999. Estimation of Temperature and Humidity Profile Information from Microwave Radiances over Different Surface Types. J. Appl. Meteor. Climatol. 38, 1526–1541. URL: `10.1175/1520-0450(1999)038<1526:EOTAHP>2.0.CO;2`.

English, S.J., Hewison, T.J., 1998. Fast generic millimeter-wave emissivity model. Proc. SPIE 3503, 288–300. doi: `10.1117/12.319490`.

Eresmaa, R., Letertre-Danczak, J., Lupu, C., Bormann, N., McNally, A., 2017. The assimilation of cross-track infrared sounder radiances at ECMWF. Q.J.R.Meteorol.Soc. 143, 3177–3188. doi: `10.1002/qj.3171`.

Eriksson, P., Ekelund, R., Mendrok, J., Brath, M., Lemke, O., Buehler, S.A., 2017. A general database of hydrometeor single scattering properties at microwave and sub-millimetre wavelengths. Earth Syst. Sci. Data 10, 1301–1326. doi: `10.5194/essd-10-1301-2018`.

Eriksson, P., Kaur, I., Pfreundschuh, S., 2020. Study to support the definition of Arctic Weather Satellite (AWS) high frequency channels. EUMETSAT Contract EUM/CO/20/4600002417/CJA Final Report , 41ppURL: `https://research.chalmers.se/en/publication/519309`.

Evans, K.F., Stephens, G.L., 1995. Microwave Radiative Transfer through Clouds Composed of Realistically Shaped Ice Crystals. Part II: Remote Sensing of Ice Clouds. J. Atmos. Sci. 52, 2058–2072. doi: `10.1175/1520-0469(1995)052<2058:MRTTCC>2.0.CO;2`.

Geer, A., Ahlgrimm, M., Bechtold, P., Bonavita, M., Bormann, N., English, S., Fielding, M., Forbes, R., Hogan, R., Hólm, E., Janiskova, M., Lonitz, K., Lopez, P., Matricadi, M., Sandu, I., Weston, P., 2017. Assimilating observations sensitive to cloud and precipitation. ECMWF Technical Memorandum 815, 60pp. doi: `10.21957/sz7cr1dym`.

Geer, A., Baordo, F., Bormann, N., English, S., 2014. All-sky assimilation of microwave humidity sounders. ECMWF Technical Memorandum No. 741, 57pp. doi: `10.21957/obosmx154`.

Geer, A., Bauer, P., Lopez, P., 2010. Direct 4D-Var assimilation of all-sky radiances. Part II: Assessment. ECMWF Technical Memorandum No.619, 29pp. doi: `10.21957/lb3he29s`.

Geer, A.J., 2021. Physical characteristics of frozen hydrometeors inferred with parameter estimation. Atmospheric Measurement Techniques 14, 5369–5395. doi: `10.5194/amt-14-5369-2021`.

Geer, A.J., Bauer, P., Lonitz, K., Barlakas, V., Eriksson, P., Mendrok, J., A. Doherty, J.H., Chambon, P., 2021. Bulk hydrometeor optical properties for microwave and sub-millimetre radiative transfer in RTTOV-SCATT v13.0. Geosci Model Dev 14, 7497–7526. doi: `10.5194/gmd-14-7497-2021`.

Geer, A.J., Lupu, C., Duncan, D., Bormann, N., English, S., 2024. SURFEM-ocean microwave surface emissivity evaluated. ECMWF Technical Memorandum doi: `10.21957/0af49d82e2`.

Hilton, F., Collard, A., Guidard, V., Randriamampianina, R., Schwaerz, M., 2009. Assimilation of IASI radiances at European NWP centres. Proceedings of the ECMWF/EUMETSAT NWP-SAF Workshop on the assimilation of IASI in NWP, May 2009 URL: `https://www.ecmwf.int/sites/default/files/elibrary/2009/9896-assimilation-iasi-radiances-european-nwp-centres.pdf`.

Kaur, I., Eriksson, P., Pfreundschuh, S., Duncan, D.I., 2021. Can machine learning correct microwave humidity radiances for the influence of clouds? Atmospheric Measurement Techniques 14, 2957–2979. doi: `10.5194/amt-14-2957-2021`.

Kazumori, M., English, S.J., 2015. Use of the ocean surface wind direction signal in microwave radiance assimilation. Quart. J. Roy. Meteor. Soc. 141, 1354–1375. doi: `10.1002/qj.2445`.

Kilic, L., Prigent, C., Jimenez, C., 2023. Development of the SURface Fast Emissivity Model for Ocean (SURFEM-ocean) based on the PARMIO radiative transfer model. Earth and Space Science 10, e2022EA002785. doi: `10.1029/2022EA002785`.

Lean, K., Bormann, N., Healy, S., 2021. Calibration of EDA spread and adaptation of the observation error model. ESA Contract 4000130590/20/NL/IA Technical Note 2 URL: `https://www.ecmwf.int/node/20302`, doi: `10.21957/1auh0nztg`.

Lean, K., Bormann, N., Healy, S., 2022a. Developing a flexible system to simulate and assimilate small satellite data. ESA Contract 4000130590/20/NL/IA Technical Note 3 URL: `https://www.ecmwf.int/node/20303`, doi: `10.21957/kjmxyh9xy`.

Lean, K., Bormann, N., Healy, S., 2023. Evaluation of future EPS-Sterna constellations with 50 and 183 GHz. EUMETSAT Contract Report, EUM/CO/22/4600002673/SDM doi: `10.21957/0a695fcc39`.

Lean, K., Bormann, N., Healy, S., English, S., 2022b. Final Report: Study to assess earth observation with small satellites and their prospects for future global numerical weather prediction. ESA Contract 4000130590/20/NL/IA Final Report URL: `https://www.ecmwf.int/en/elibrary/8132`

4-final-report-study-assess-earth-observation-small-satellites-and -their-prospects, doi: 10.21957/kp7z1sn1n.

Salonen, K., McNally, A., 2019. Enhancing the hyperspectral infrared radiance assimilation in the ECMWF system. Presentation at ITSC-22, Saint-Sauveur, Canada URL: https://itwg.sse c.wisc.edu/wordpress/wp-content/uploads/2023/05/9.02.salonen_itsc22 .pdf.

Turner, E., Fox, S., Mattioli, V., Cimini, D., 2022. Literature review on microwave and sub-millimetre spectroscopy for MetOp Second Generation. NWP-SAF report, NWPSAF-MO-TR-039 , 101ppURL: https://nwp-saf.eumetsat.int/site/download/members_docs/cdop-3_ref erence_documents/NWPSAF_report_submm_litrev.pdf.

Wang, D., Prigent, C., Kilic, L., Fox, S., Harlow, C., Jimenez, C., Aires, F., Grassotti, C., Karbou, F., 2017. Surface Emissivity at Microwaves to Millimeter Waves over Polar Regions: Parameterization and Evaluation with Aircraft Experiments. J. Atmos. Oceanic Technol. 34, 1039–1059. doi: 10.117 5/JTECH-D-16-0188.1.

Weng, F., 2011. Observations and simulations of microwave land emissivity. Conference Paper, ECMWF-JCSDA Workshop on Assimilating Satellite Observations of Clouds and Precipitation into NWP Models, Shinfield Park, Reading, 15-17 June 2010 URL: https://www.ecmwf.int/en /elibrary/74531-observations-and-simulations-microwave-land-emissiv ity.

Weston, P., Bell, W., Eyre, J., 2014. Accounting for correlated error in the assimilation of high-resolution sounder data. Quart. J. Roy. Meteorol. Soc. 140, 2420–2429. doi: 10.1002/qj.2306.